



FABIAN: A daily product of Fractional Austral-summer Blue Ice over Antarctica during 2000–2021 based on MODIS imagery using Google Earth Engine

Zhongyang Hu^{a,*}, Peter Kuipers Munneke^a, Stef Lhermitte^b, Mariel Dirscherl^c, Chaonan Ji^{c,d}, Michiel van den Broeke^a

^a Institute for Marine and Atmospheric research Utrecht (IMAU), Utrecht University, Princetonplein 5, Utrecht 3584 CC, the Netherlands

^b Department of Geoscience & Remote Sensing, Delft University of Technology, Building 23, Stevinweg 1, Delft 2628CN, the Netherlands

^c German Remote Sensing Data Center (DFD), German Aerospace Center (DLR), Muenchener Str. 20, Wessling 82234, Germany

^d Applied Geoinformation Science Lab, Geography Department, Humboldt Universitaet zu Berlin, Unter den Linden 6, Berlin 10099, Germany

ARTICLE INFO

Edited by Menghua Wang

Keywords:

Blue ice

Antarctica

MODIS

Spectral mixture analysis

Google Earth Engine

ABSTRACT

Antarctic blue ice areas are exposed due to erosion and sublimation of snow. At the same time, surface melt can form surface types that are spectrally similar to blue ice, especially at low elevations. These are termed melt-induced blue ice areas. Both types of blue ice are sensitive indicators of climate change. Satellite remote sensing is a powerful technique to retrieve the spatial extent of blue ice areas and their variation in time. Yet, existing satellite-derived blue ice area products are either mono-temporal for the entire Antarctic ice sheet, or multi-temporal for a limited area. Here, we present FABIAN, a product of blue ice fraction over Antarctica, derived from the moderate resolution imaging spectroradiometer (MODIS) archive covering the period 2000–2021. A spectral mixture analysis (SMA) in Google Earth Engine, based on a careful selection of end-member spectra, accurately reconstructs the reflectance observed by MODIS in blue ice areas. Based on a validation with contemporaneous Sentinel-2 images, FABIAN has a root mean square error in blue ice fraction of approximately 10% ~ 20% in wind-induced blue ice areas, and 20% ~ 30% in melt-induced blue ice areas across six selected test sites in the coastal East Antarctic ice sheet. FABIAN is challenged in regions with shallow melt streams and lakes, since their spectral profiles are similar to those from blue ice areas in MODIS bands. For further analyses and applications, FABIAN holds the potential for (1) deriving annual blue ice area maps, (2) distinguishing between wind- and melt-induced blue ice types, (3) evaluating and correcting (regional) climate models, and (4) analyzing temporal variations in blue ice abundance and exposure.

1. Introduction

Blue ice areas cover about 1% of the Antarctic ice sheet (Winther et al., 2001; Bintanja, 1999). It is ancient ice with a peculiar blue and rippled appearance that surfaces after the firn layer has been removed (Bintanja, 1999). Traditionally, blue ice has been defined as a surface type occurring at locations with a negative surface mass balance, where wind erosion and sublimation is larger than accumulation (Bintanja, 1999). In this study, blue ice areas of this origin are referred to as wind-induced blue ice areas. However, Winther et al. (2001) added a second type, so-called melt-induced blue ice areas, being (patchy) bare ice with a bluish appearance experiencing cyclic melt-freeze processes (Winther,

1994; Liston et al., 1999), mainly due to surface melt and katabatic winds. The origin of this ice is not glacial, but due to melt, refreezing and horizontal water transport. When observed from space, ‘melt-induced blue ice’ also includes surfaces other than ice, like slush, refrozen supraglacial lakes, because they cannot be discriminated based on their optical spectra. In Antarctica, blue ice areas are located in coastal and/or in mountainous regions. Blue ice areas are sensitive to climate change (Orheim and Lucchitta, 1990; Bintanja, 1999), therefore, they have often been studied in a paleoclimatological context (Sinisalo and Moore, 2010). On decadal timescales, most wind-induced blue ice areas appear to be very stable (Bintanja, 1999; Sinisalo and Moore, 2010). Bintanja and Van den Broeke (1995a, 1995b) confirmed the stability of wind-

* Corresponding author.

E-mail address: z.hu@uu.nl (Z. Hu).

<https://doi.org/10.1016/j.rse.2022.113202>

Received 14 February 2022; Received in revised form 25 July 2022; Accepted 26 July 2022

Available online 9 August 2022

0034-4257/© 2022 The Authors. Published by Elsevier Inc. This is an open access article under the CC BY license (<http://creativecommons.org/licenses/by/4.0/>).

induced blue ice areas near nunataks in Dronning Maud Land. [Ligtenberg et al. \(2014\)](#) explained variations in the Byrd Glacier blue ice area as a result of the interaction between ice velocity, surface mass balance, and the upstream firn mass. However, the precise dynamics of blue ice area formation and variation across the entire Antarctic ice sheet remain ambiguous, and require first a more robust inventory of blue ice areas. Revealing these patterns would contribute to our understanding of the variability in the surface radiation and energy budget, and thereby of temperature, and possibly surface melt.

Spaceborne remote sensing is the backbone for mapping the areal extent of blue ice areas, with practical applications such as mapping meteorite searching areas ([Tollenaar et al., 2022](#)) and potential airfield locations ([Mellor and Swithinbank, 1989](#); [Yoshida et al., 1971](#)). It is primarily based on multispectral optical data, thanks to the unique spectral profile of blue ice areas compared to its ambient environment of snow and/or rock. Its history can be traced back to 1976, when the national institute of polar research in Tokyo, Japan, delineated blue ice areas in the Yamato Mountains, Antarctica, using a Landsat 1 (previously known as the Earth resources technology satellite-1, ERTS-1) scene ([Williams et al., 1982](#)). Since the concept of band (ratio) thresholding was proven to be suitable for mapping blue ice areas ([Orheim and Lucchitta, 1988, 1990](#)), it has become a frequently used approach for detecting blue ice areas in optical imagery ([Brown and Scambos, 2004](#); [Hui et al., 2014](#); [Winther et al., 2001](#); [Bronge and Bronge, 1999](#)). The first blue ice area map for the entire continent made use of an image mosaic from the national oceanic and atmospheric administration - advanced very high resolution radiometer (NOAA-AVHRR) ([Winther et al., 2001](#)). A pan-Antarctic map of blue ice areas at higher resolution was presented by [Hui et al. \(2014\)](#), based on the 30 m resolution Landsat image mosaic of Antarctica (LIMA) product ([Bindschadler et al., 2008](#)). Apart from these optical products, blue ice area mapping has also been attempted with radar imagery ([Liu et al., 2006](#); [Cheng et al., 2003](#)), yet at local to regional scale only.

To date, spaceborne observations of the intra-and inter-annual variability of Antarctic-wide blue ice are still missing. To our knowledge, all Antarctic-wide blue ice area products are static and derived from a multi-year mosaic of satellite images. Intra-and inter-annual variability of blue ice areas is thereby neglected, although it was shown to occur ([Brown and Scambos, 2004](#)), as snow/ice surfaces can be highly dynamic. Cloud obstruction can hamper a correct interpretation, since it directly poses a challenge for assessing spatiotemporal variability in Antarctic blue ice areas, especially using (semi-)high resolution optical satellite images (e.g., Sentinel-2 and Landsat). Within an austral summer, it is unfeasible for the Sentinel-2 and/or Landsat constellations to acquire sufficient and adequate cloud-free observations for a proper analysis of intra-annual blue ice dynamics. In contrast, the moderate resolution imaging spectroradiometer (MODIS), observing the same place twice a day with Terra and Aqua, holds a great potential to reveal intra-annual blue ice dynamics. A temporally resolved product of blue ice area coverage also allows us to highlight different dynamics of wind- and melt-induced blue ice areas. They form by very different mechanisms, and their dynamics and anomalies express changes and variability of climatic drivers on different timescales. Melt-induced blue ice areas are very dynamical and sensitive to short-term variations in the changing ambient environment, especially surface melt. In this regard, identifying these two types of blue ice can further improve our understanding of the changing climate over Antarctica.

This study develops a daily product of fractional austral-summer blue ice over Antarctica (FABIAN). Fractional blue ice refers to the percentage of blue ice located within a MODIS pixel at a given time. FABIAN is based on MODIS images acquired during the austral summers from 2000/01 to 2020/21, and can easily be extended each year. FABIAN is able to reveal intra-and inter-annual variability at daily

resolution, thereby strongly enhancing our monitoring capacity of blue ice areas. FABIAN makes use of linear spectral mixture analysis (SMA), a well-developed technique for estimating land cover fractions. Presently, SMA has been applied frequently to vegetated and urbanized areas ([Somers et al., 2011](#); [Wu and Murray, 2003](#); [Elmore et al., 2000](#); [Smith et al., 1990](#)) but also in snow/ice-covered areas ([Hu et al., 2017](#); [Vikhamar and Solberg, 2003](#)). SMA models the observed reflectance by combining the spectra of pure, single-type land covers (called endmembers) from a certain pixel. These endmembers are weighted by their fractional coverage ([Smith et al., 1990](#)). Antarctica is a particularly interesting area for SMA applications, since the variety of land surface forms is more limited than in vegetated and urbanized areas, reducing the number of endmembers required for a reliable retrieval. [Section 2](#) introduces the overall framework of FABIAN, the methods we apply for estimating the blue ice fraction, our validation setup, as well as the data sets we use. In [Section 3](#), we present and discuss the results of FABIAN, focusing on dynamics of the blue ice fraction estimates from FABIAN, and the relation to meteorological parameters provided by a polar regional atmospheric climate model (RACMO2). Next, we evaluate the blue ice fraction results from FABIAN, as well as the quality of the reference blue ice fraction data set derived from Sentinel-2 images. In the end, we summarize the development of FABIAN and its application.

2. Methods and materials

A flowchart of FABIAN generation is shown in [Fig. 1](#). The framework consists of three principal steps: (I) the construction of a spectral library for the SMA; (II) a MODIS-based SMA procedure to estimate a gridded blue ice fraction map; (III) evaluation of the blue ice fraction maps using contemporaneous Sentinel-2 imagery. In part I (block I in [Fig. 1](#)), the hyperspectral data (from optical radiative transfer model simulations, and field or laboratory measurements) are radiometrically resampled and inserted, with candidate multispectral endmembers derived from MODIS imagery, into the initial spectral library. The representativeness of the endmembers is assessed using two independent methods, i.e., EMC: endmember average root mean square error ([Dennison and Roberts, 2003](#)); minimum average spectral angle ([Dennison et al., 2004](#)); count based endmember selection ([Roberts et al., 2003](#)), and AMUSES: automated music and spectral separability-based endmember selection ([Degerickx et al., 2017](#)). Subsequent endmember selection based on the EMC and AMUSES outputs then yields the seven most representative endmembers, and they are selected for the final spectral endmember library. The represented surface types are: (1) blue ice, (2) coarse-grained snow, (3) fresh snow, (4) bare rock, (5) deep water, (6) slush, and (7) wet snow. These selected endmembers are then used for SMA of MODIS images (block II in [Fig. 1](#)). Temporal gaps (mostly due to cloud obstructions) in SMA-estimated blue ice fraction results are then filled with weekly or monthly mean pixel value. Meanwhile, we classified the contemporaneous Sentinel-2 scenes into blue ice area maps using the Otsu method ([Otsu, 1979](#)) to produce the blue ice fraction validation data set. In the remainder of this subsection, we present details of the endmember selection, blue ice fraction derivation from MODIS imagery, blue ice fraction derivation from Sentinel-2 imagery, and blue ice fraction evaluation.

2.1. Satellite imagery and cloud masking

MODIS has been providing continuous observations of the Earth's surface for more than two decades. In this study, we used the seven surface reflectance bands (1: 620–670 nm, 2: 841–876 nm, 3: 459–479 nm, 4: 545–565 nm, 5: 1230–1250 nm, 6: 1628–1652 nm, and 7: 2105–2155 nm) from the MOD09GA (MODIS/Terra Surface Reflectance Daily L2G Global 1 km and 500 m SIN Grid) and MYD09GA (MODIS/

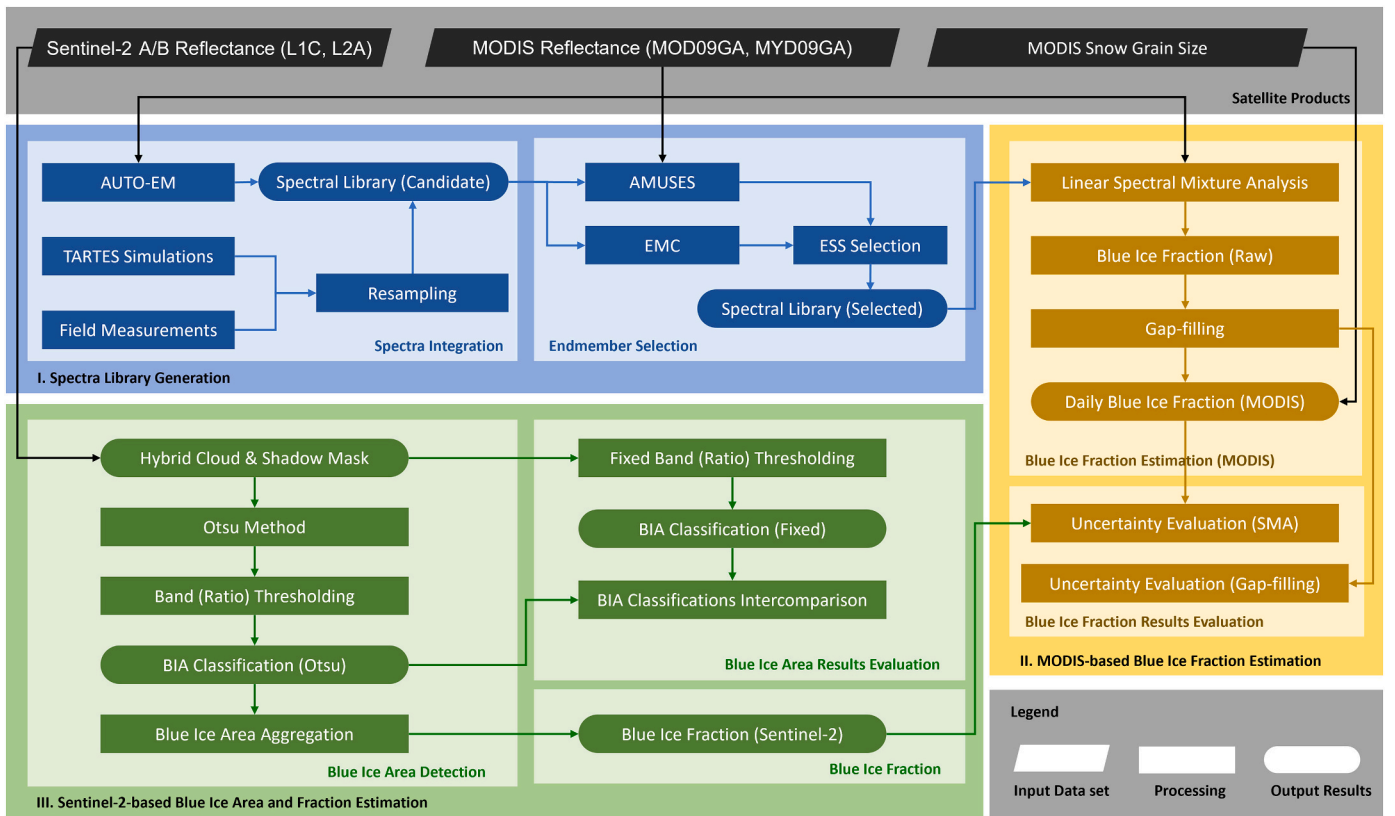


Fig. 1. Overall flowchart illustrating the employed data sets, methods, and the corresponding intercomparisons and evaluations.

Aqua Surface Reflectance Daily L2G Global 1 km and 500 m SIN Grid products archived in Google Earth Engine (GEE; Gorelick et al., 2017) as the reflectance input for SMA, in which cloud pixels were masked out based on the '1 km Reflectance Data State' band. To assess the SMA-estimated blue ice fraction results, we used optical remote sensing products from Sentinel-2, including L2A bottom of atmosphere reflectance (for blue ice area classification) and L1C top of atmosphere reflectance (for cloud and shadow detection). These data are not available daily, but have the advantage of a much higher spatial resolution of ~ 20 m. Over the Antarctic continent, the current two-satellite constellation of the Copernicus Sentinel-2 mission records land surface changes every 2–3 days under cloud-free conditions. In GEE, Sentinel-2 L2A products over Antarctica are available since 2018; therefore, the Sentinel-2 L2A and L1C images that we use in this study, were acquired partially in austral summer 2018/19 and entirely in austral summers 2019/20 and 2020/21.

To mask out clouds in Sentinel-2 images, we establish the best cloud masking algorithm for Antarctic conditions. There exist several ways for cloud masking of Sentinel-2 images in GEE, including (1) SCL (a scene classification map), (2) s2cloudless (available on <https://medium.com/sentinel-hub/improving-cloud-detection-with-machine-learning-c09dc5d7cf13>, accessed on 02 August 2021), (3) modified s2cloudless (available on <https://developers.google.com/earth-engine/tutorials/community/sentinel-2-s2cloudless>, accessed on 02 August 2021), and (4) a machine-learning-based method developed by the German research centre for geosciences (referred to as GFZ method; Hollstein et al., 2016). We demonstrate the results from these four algorithms under three scenarios (i.e., remote sensing images appearing fully hazy with optically thin layer of clouds, partially cloudy/hazy, and heavily cloudy) in the Queen Fabiola Mountains, Dronning Maud Land (Fig. A.14). SCL is the least accurate cloud mask in identifying clouds, water, and shadows, resulting in inaccurate cloud shadow detection using the modified s2cloudless which relies on SCL outcomes.

S2cloudless is the most accurate in detecting clouds, and the GFZ provides the most accurate cloud shadow masks. Therefore, we decide to create a hybrid cloud masking scheme combining the cloud mask from s2cloudless and the cloud shadow mask from the GFZ method.

2.2. Candidate endmember spectra collection and simulation

In order to implement SMA, a spectral library consisting of spectra representing the potential types of land cover (i.e., endmembers) for the study area is indispensable. Conventionally, endmembers can be acquired from remote sensing images, field/laboratory measurements, and simulations. In this study, we first collected hyperspectral measurements from earlier publications of field or laboratory work (Hui et al., 2014; Zatko and Warren, 2015; Hannula et al., 2020), and from the spectral library ECOSTRESS (previously known as the ASTER spectral library; Meerdink et al., 2019). Given that all these candidate spectra are hyperspectral, they were resampled to MODIS band configurations using the 'hsdar' package in R (<https://cran.r-project.org/web/packages/hsdar/hsdar.pdf>, accessed on 02 August 2021). These spectra are used to build the initial spectral library (block I spectra integration in Fig. 1).

We expanded the initial spectral library by using two additional sources of spectra. The first source is TARTES, a two-stream radiative transfer model for light in snow (Libois et al., 2013), from which we generated snow spectra. TARTES is a fast optical radiative transfer model used to compute the spectral albedo of a snowpack, defined as a set of homogeneous horizontal layers of snow with a specific surface area (SSA), density, impurities, and grain shape. For this study, we modeled the spectral albedo of a 10 m snowpack consisting of spherical grains with a constant density of $300 \text{ kg}\cdot\text{m}^{-3}$, and no impurities. For fresh snow spectra, the optical diameter of the spherical snow grains varied between 60 and $210 \mu\text{m}$. For coarse-grained snow, the diameter varied between 750 and $1500 \mu\text{m}$. The second source for candidate endmember spectra was derived from multi-temporal MODIS images

using the four-step automatic endmember extractor (hereinafter noted as AUTO-EM) developed in GEE. First, AUTO-EM classifies cloud-free pixels in a MODIS image into blue ice, bare rock, deep water, and slush based on published methods (summarized in Table B3). To enhance classification accuracy, we tightened some thresholds (indicated by * in Appendix B) suggested by the original methods. This may underestimate the areal extent of a certain class but increase the reliability of the classification. Second, to capture the most stable pixel of a certain class, we selected the pixel with the highest frequency classified as the target class during the austral summers between 2000/01 and 2020/21. This procedure was carried out separately for the months December, January and February, in order to allow for temporal variations. An overview of all collected endmembers is summarized by land cover type in Table 1. Third, these spectra are inserted into the initial spectral library, together with the resampled spectra originated from TARTES simulations, and field or laboratory measurements.

2.3. Endmember selection and spectral library generation

The total number of endmember spectra for the SMA needs to be reduced to $n + 1$, where n is the number of bands in the input imagery, due to the mathematical principle and ‘sum-to-one’ constraint of SMA. To arrive at a final selection of endmembers from the candidate spectra described above, we made use of two scoring techniques called EMC and AMUSES (automated music and spectral separability based endmember selection). EMC is a combination of EAR (endmember average root mean square error; Dennison and Roberts, 2003), MASA (minimum average spectral angle; Dennison et al., 2004), and CoB (count based endmember selection; Roberts et al., 2003). The other technique is AMUSES, which stands for automated music and spectral separability-based endmember selection (Degerickx et al., 2017). To combine these two metrics for the endmember selection, we developed our own endmember selection score (ESS). The ESS of a selected endmember e_s (ESS_{e_s}) is calculated as the weighted sum of the min-max normalized EMC indices ($EAR_{e_s,c}$, $MASA_{e_s,c}$, and CoB_{in,e_s} : CoB within its own class) within a certain spectrum/land cover class c , and $AMUSES_{e_s}$ outcomes, according to Eqs. (1)–(2):

$$x' = \frac{x - \min(x)}{\max(x) - \min(x)}, \quad (1)$$

$$ESS_{e_s,c} = 0.2 \times (EAR'_{e_s,c} + MASA'_{e_s,c} + (1 - CoB'_{in,e_s})) + 0.4 \times (1 - AMUSES'_{e_s}), \quad (2)$$

where x' is the min-max normalized endmember selection index (x). The weights are manually signed to balance the EMC scores and AMUSES score, as well as each EAR, MASA, and CoB within the EMC scores. Meanwhile, slightly more focus is given on EMC scores to guarantee a better spectral representativeness within the spectral library.

In this way, we selected the most representative spectrum for the following surface types: (1) blue ice, (2) coarse-grained snow, (3) fresh

snow, (4) bare rock, (5) deep water, (6) slush, and (7) wet snow, as the selected endmembers for spectral mixture analysis inputs for the entire Antarctica. The selected spectra with the highest scores are the most (intra-and inter-class) representative ones within the initial spectra library (according to EMC), as well as in the real MODIS images (according to AMUSES). In terms of water and slush, their spatial patches can be larger. Therefore, it is easier to obtain pure pixels in the satellite images. Compared with the water endmember from ECOSTRESS, the satellite-image-derived ones are more representative within the initial spectral library and in the real MODIS images. When it comes to snow endmembers, identifying fresh/coarse-grained/wet snow spectra from satellite images is very challenging. For pure fresh and coarse-grained snow surfaces, we deem the simulated spectra to be the state-of-the-art, since their optical properties are very well understood theoretically. Yet, for wet snow, it is also challenging to model it using radiative transfer model, such as TARTES. Therefore, the ground measurement is more well-suited. The only case, when manual interference is implemented, is selecting the best bare rock endmember. After the visual inspection and analysis, we selected the rock spectrum measured in the field campaign (Hui et al., 2014) with the second-highest ESS instead of the highest-ESS one. The reason is that the rock endmember of the highest ESS is derived using AUTO-EM from MODIS imagery. However, its spectral profile is contaminated by other endmembers, most likely snow, which disagrees with the definition of the endmember. Such a phenomenon often appears in a 500×500 m MODIS rock pixel and makes AUTO-EM erroneously identifying it as the most stable rock endmember. The spectra in the final library are shown in Fig. 2, and the full table EMC, MASA, CoB, and ESS results are available on <https://doi.org/10.5281/zenodo.6624077> (accessed on 8 June 2022).

2.4. Spectral mixture analysis (SMA) for estimating blue ice fraction

The fraction of blue ice area in each daily MODIS observation of the Antarctic continent is computed using SMA. To accelerate data processing, we first excluded areas having a snow grain size of $< 400 \mu\text{m}$, assuming that these are areas without blue ice (Hui et al., 2014). Second, cloud-free pixels from MODIS Terra and Aqua were combined. If both satellites return a cloudy pixel for a particular day, we take the mean pixel value from a 6-day window centered around it. For a very limited amount of pixels (Fig. 3), remaining gaps had to be filled with the mean pixel value from a 30-day window around that day. In linear SMA, the spectral properties of a pixel are modeled as a linear combination of endmember spectra weighted by their corresponding fractional abundance (Roberts et al., 1998; Smith et al., 1990). Mathematically, linear SMA can be described as below:

$$\rho_b = \sum_{i=1}^N (f_i \times e_{i,b}) + \varepsilon_b, \quad (3)$$

$$\sum_{i=1}^N f_i = 1, \quad (4)$$

where ρ_b is the observed reflectance of a certain pixel in band b , f_i is the fractional abundance of the i^{th} endmember (e_i), $e_{i,b}$ is the reflectance of e_i in band b , N represents the total number of endmembers, and ε_b stands for residuals of the linear fit in band b . Finally, we add the computed slush fraction to the blue ice fraction, because most slush areas agree with the definition of melt-induced blue ice areas by Winther et al. (2001), given their thaw-frozen cycle and blue appearance.

2.5. Generation of the Sentinel-2-derived evaluation data set

For an evaluation of the MODIS-based blue ice fraction, we generate a set of Sentinel-2-derived high-resolution blue ice area maps across six test sites. After applying the cloud mask, blue ice areas are mapped using band (ratio) thresholding, the leading method in blue ice area mapping

Table 1

The number of spectra obtained from different sources: TARTES simulations, automatic endmember extractor (AUTO-EM), and field/laboratory measurements from ECOSTRESS (Meerdink et al., 2019), Hui et al. (2014), Hannula et al. (2020), and Zatko and Warren (2015).

	TARTES	AUTO-EM	Field Measurement
Fresh Snow	6	–	2
Medium-grained Snow	–	–	1
Coarse-grained Snow	6	–	1
Wet Snow	6	–	2
Blue Ice	–	18	1
(Deep) Water	–	9	1
Slush	–	18	3
Bare Rock	–	18	1

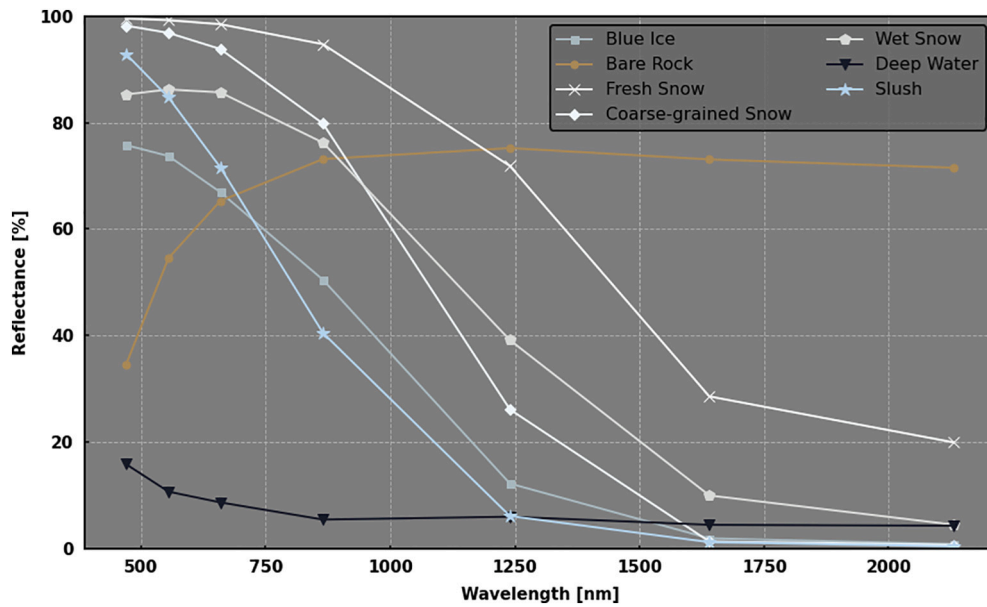


Fig. 2. Overview of endmembers in the spectral library for the spectral mixture analysis (SMA). Each endmember is coloured based on its RGB reflectance.

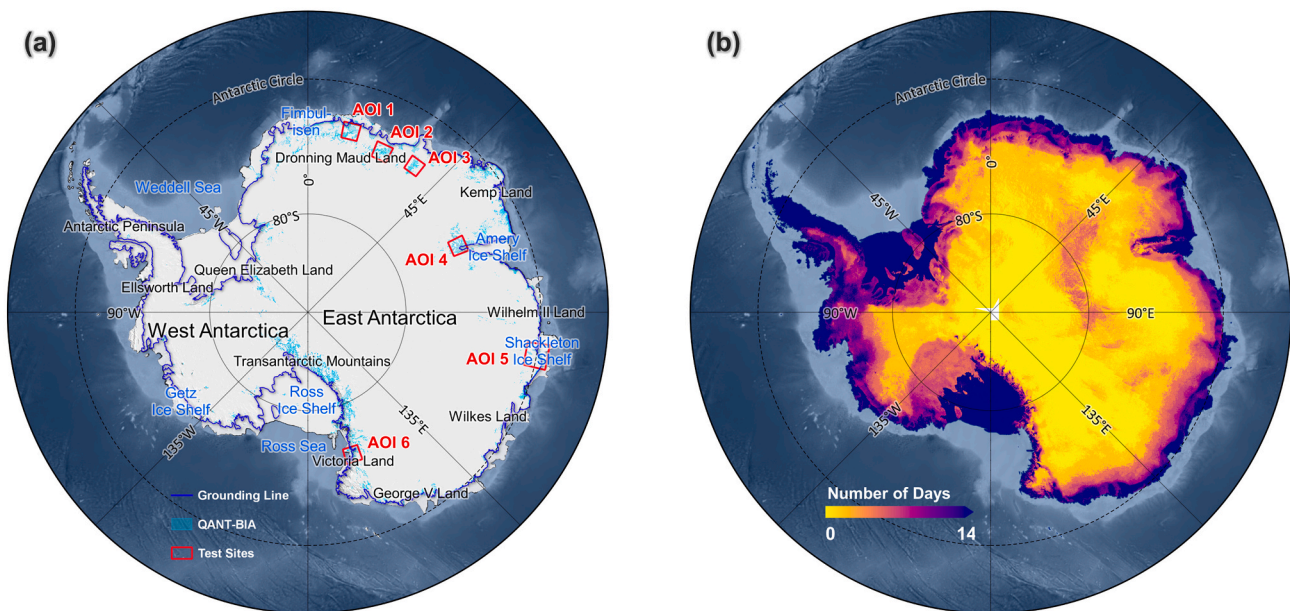


Fig. 3. Overview of the selected test areas: (a) red rectangles indicate the locations of six test areas: the Petermann Ranges (AOI 1), Sør-Rondane Mountains (AOI 2), Queen Fabiola Mountains (AOI 3), Amery Ice Shelf (AOI 4), Shackleton Ice Shelf (AOI 5), and Victoria Land (AOI 6), on a background map of blue ice areas from Quantarctica (QANT-BIA) (Matsuoka et al., 2021) based on the Landsat image mosaic of Antarctica (LIMA) product (Bindschadler et al., 2008) using the Hui et al. (2014) method, and the grounding line information is derived from Bindschadler et al. (2011); (b) the median of the number of successive days without valid observations indicates the average length of data gaps in the moderate resolution imaging spectroradiometer (MODIS) images during the austral summers 2000/01 to 2020/21. (For interpretation of the references to colour in this figure legend, the reader is referred to the web version of this article.)

at high resolution. The band ratio (BR) between band a and band b ($BR_{a,b}$) can be calculated as:

$$BR_{a,b} = \frac{\rho_a - \rho_b}{\rho_a + \rho_b}, \quad (5)$$

where ρ_a and ρ_b are the surface reflectance of band a and band b , respectively. In this study, we used the $BR_{8A,12}$ (Band 8A: near-infrared, Band 12: shortwave infrared) for Sentinel-2, which is equivalent to the $BR_{4,7}$ (Band 4: near-infrared, Band 7: shortwave infrared) for Landsat ETM+ proposed by Hui et al. (2014). Instead of using a fixed threshold,

we applied the Otsu method (Otsu, 1979) to dynamically search for an optimal threshold (th) for each Sentinel-2 image. The Otsu method determines th by maximizing the inter-class variance or minimizing the intra-class variance using exhaustive search:

$$th = \operatorname{argmax}_t \{ \delta_{inter}^2(t) \} = \operatorname{argmin}_t \{ \delta_{intra}^2(t) \}, \quad (6)$$

where $\delta_{inter}^2(t)$ and $\delta_{intra}^2(t)$ are intra- and inter-class variance under the partitions of using a different threshold t .

Finally, blue ice areas are identified in the Sentinel-2 images if: (1) the reflectance of band 1 is greater than 0.8, (2) the reflectance of band

8A is between 0.3 and 0.7, and (3) $BR_{8A, 12}$ is greater than th . We also tested the original method proposed by Hui et al. (2014) using their original of $th = 0.90$. Because the blue-ice spectral profile in VIS-NIR (visible and near infra-red) bands is very steep, the blue ice classification can be very sensitive to the value of this threshold th . Therefore, we also took an adapted threshold of $th = 0.85$. A comparison of these Hui-based methods and the Otsu-method is performed in Section 5.2. Once the blue ice areas are classified in the Sentinel-2 images, they are downscaled to the 500×500 m MODIS pixel grid. If the MODIS pixel is classified as cloudy, it will be discarded. Cloud pixels in Sentinel-2 are also excluded from the analysis.

2.6. Evaluation of blue ice fraction results

To evaluate the MODIS-derived blue ice fraction results using SMA, we analyzed the results from two perspectives: (1) the fit of the original MODIS reflectance using SMA, and (2) the accuracy of the blue ice fraction estimation. To achieve this, we use two metrics, i.e., RMSE of SMA itself ($RMSE_{REF} \in [0, 1]$ or, equivalently, $[0\%, 100\%]$) and RMSE of the SMA blue ice fraction results compared with the aggregated blue ice areas using Sentinel-2 ($RMSE_{BIF} \in [0, 1]$ or, equivalently, $[0\%, 100\%]$), which are calculated as follows:

$$RMSE_{REF} = \sqrt{\frac{\sum_{b=1}^M (\rho_b - \rho'_b)^2}{M}}, \quad (7)$$

$$RMSE_{BIF} = \sqrt{\frac{\sum_{i=1}^N (f_{SMA,i} - f_{S2,i})^2}{N}}, \quad (8)$$

where ρ_b and ρ'_b are MODIS-observed and SMA-modeled reflectance in band b , and M stands for the total number of bands which equals 6 in this study. The fractions $f_{SMA, i}$ and $f_{S2, i}$ are SMA-estimated and Sentinel-2-derived blue ice fraction of the cloud-free pixel i , and N stands for the total number of cloud-free MODIS pixels with valid contemporaneous Sentinel-2-derived blue ice fraction. $f_{S2, i}$ is calculated using the 20×20 m Sentinel-2-derived blue ice area results, which are then aggregated to blue ice fraction while matching the 500×500 m MODIS pixels. $RMSE_{REF}$ measures the performance regarding the linear fit of the endmembers to the observed reflectance. It evaluates the performance of endmember selection for a pixel. On the other hand, $RMSE_{BIF}$ measures the agreement between MODIS-derived and Sentinel-2-derived blue ice fraction.

For the development and validation of FABIAN, we identified six test areas (Fig. 3) across the Antarctic continent in different climatological settings. All of these areas are identified as blue ice areas in the Landsat-based LIMA product (Bindshadler et al., 2008). Three test areas are located in Dronning Maud Land, East Antarctica: the Petermann Ranges, the Sør-Rondane Mountains, and the Queen Fabiola Mountains. The other three areas are located on the Amery Ice Shelf, the Shackleton Ice Shelf, and in Victoria Land.

2.7. Auxiliary data

For the generation and evaluation of the blue ice fraction calculations, we used five auxiliary data sets: (1) a MODIS-based snow grain size product (Scambos et al., 2007) which is used to mask out non-blue ice areas; (2) Sentinel-2-based supraglacial lake extents (Dirscherl et al., 2021), which provide a time-series information on the evolution of supraglacial lakes in blue ice areas; (3) meteorological parameters (i.e., 2 m temperature, wind speed, sublimation, surface melt, and snowfall) simulated by the regional climate model RACMO version 2.3p2 (Van Wessem et al., 2018), which is used to interpret blue ice variation in terms of climatological and meteorological drivers. RACMO2 is

demonstrated to have an excellent simulation of surface mass balance over a wide range of climatological conditions (Van Wessem et al., 2018), surface meteorology (van Wessem et al., 2015), and in predicting the location of wind-induced blue ice areas (van den Broeke et al., 2006); (4) a 90 m digital elevation model (TanDEM-X 90 m DEM; Rizzoli et al., 2017) provided by the German aerospace center (DLR), which helps in identifying nunataks and topographical features in blue ice areas; and (5) blue ice areas from Quantarctica (Matsuoka et al., 2021) based on the LIMA product (Bindshadler et al., 2008) using the Hui et al. (2014) method (hereafter referred to as QANT-BIA).

3. Results and discussion

3.1. Overall blue ice dynamics characterized by FABIAN

FABIAN provides daily blue ice fractions at the MODIS pixel level (500×500 m) during austral summers 2000/01 to 2020/21. It is a more up-to-date blue ice product providing pixel-based blue ice fraction (numeric) information, compared to previous static mono-temporal blue ice maps which provides binary information on a pixel level. Such a long-term daily blue ice fraction information also allows the detection of intra- and inter-annual variation of blue ice. We take the median of summertime blue ice fraction as a measure for annual blue ice abundance, and the coefficient of variation to assess blue ice exposure. The spatial patterns of median blue ice fraction and coefficient of variation, based on all austral summer data between 2000/01 and 2020/21, are displayed in Fig. 4. In general, the location and extent of areas with high median blue ice fractions agree with the blue ice areas from QANT-BIA (shown as purple outlines). It indicates that the median blue ice fraction can be used as a proxy for blue ice area detection (e.g., based on simple thresholding). Also, on a regional scale (Fig. 4b, e, h, and k), the median blue ice fraction is useful to delineate blue ice areas. The best agreement ($\sim 89\%$) in blue ice areas between FABIAN (with larger than 50% blue ice fraction) and QANT-BIA is found in the Queen Fabiola Mountains whose blue ice areas are mostly wind-induced (according to Winther et al. (2001)). In the rest of the selected regions in Fig. 4, FABIAN is more likely to underestimate than overestimate blue ice areas, especially in the Petermann Ranges. This is most likely due to the elevation difference and mechanisms of blue ice area formation (i.e., erosion, sublimation, surface melt, and wind) between wind-induced and melt-induced blue ice areas. The northern part of the Petermann Ranges is situated at low elevations, which leads to possible surface melt during austral summer. The southern parts, however, are mostly wind-induced blue ice areas near summits/nunataks (shown as brown triangles in Fig. 4, which are identified by the geographic names information system developed by the United States geological survey), which are exposed to strong winds. Melt-induced blue ice areas are formed due to surface melt that occurs episodically. Therefore, the FABIAN median blue ice fraction in these melt-induced blue ice areas is often lower than in wind-induced blue ice areas. The only exception is observed in the middle of large melt-induced blue ice areas, over which blue ice fraction is high (particularly on ice shelves). In large melt-induced areas at low elevations zones, Winther et al. (2001) found the concentration of ice-bound snow crystals increases after melt-freeze cycles, resulting in an increment in surface albedo. While melt water and/or debris may present constantly in the center of these large melt-induced blue ice areas, which maintains the spectral similarity to wind-induced blue ice.

As a proxy of blue ice exposure, the geographical variation of the coefficient of variation is also shown in Fig. 4. There is a negative correlation between the median blue ice fraction and its temporal coefficient of variation. Given the blue ice classification produced by Winther et al. (2001), the areas with high coefficients of variation are mostly melt-induced blue ice areas, melt streams, ponds/lakes, as well as edges of wind-induced blue ice areas. Blue ice fractions within these areas are more variable during an austral summer, because these surfaces tend to change rapidly from one type to another. For example, a snow surface

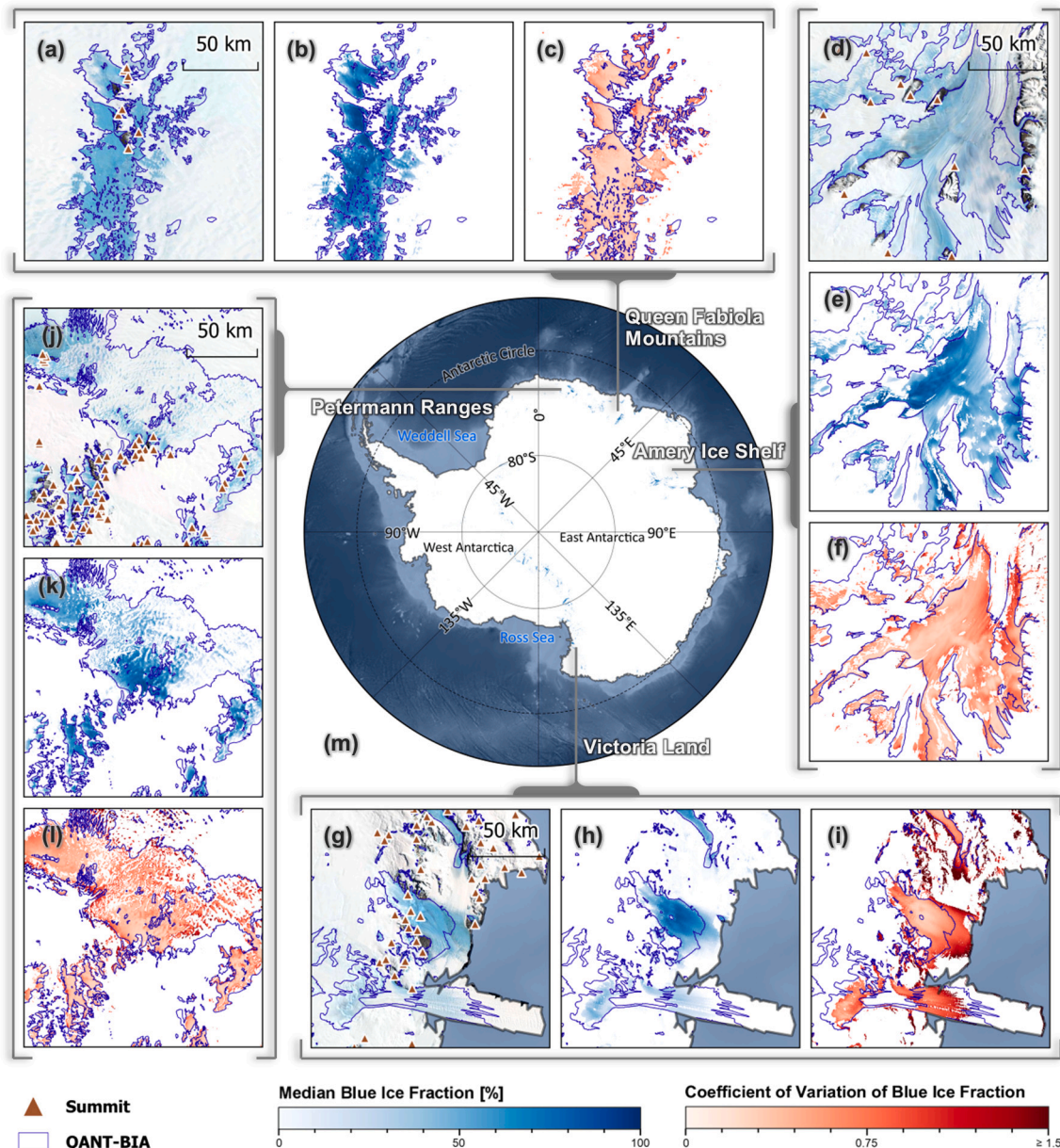


Fig. 4. Median blue ice fraction in the austral summers between 2000/01 and 2020/21 (m). Detailed maps from (b) the Queen Fabiola Mountains, (e) Amery Ice Shelf, (h) Victoria Land, and (k) Petermann Ranges. The corresponding coefficient of variation is shown in panels (c, f, i, l). The background images (a, d, g, j) of each zoom-ins are from the Landsat image mosaic of Antarctica (LIMA) product (Bindschadler et al., 2008). The dark blue solid lines delineate the blue ice areas from Quantarctica (QANT-BIA) (Matsuoka et al., 2021) based on the LIMA product (Bindschadler et al., 2008) using the Hui et al. (2014) method. (For interpretation of the references to colour in this figure legend, the reader is referred to the web version of this article.)

can turn to slush and further to blue ice due to melt, leading to shallow melt features. Moreover, snowfall-induced blue ice fraction fluctuations last longer in melt-induced blue ice areas than in wind-induced blue ice areas, due to the relatively low wind speed to remove the fresh snow, and the subsequent formation of superimposed (refrozen) ice and/or wet snow layers. Besides, after snowfall, melted blue ice may transform back to frozen ice as temperature drops. Therefore, the coefficient of variation of blue ice fraction in these blue ice areas is high (details see Fig. 9). In contrast, wind-induced blue ice areas show low coefficients of variation of blue ice fraction (Fig. 4c, f, i, and l). Inter-annual variations of wind-induced blue ice areas are mainly triggered by the changes in wind patterns and snowfall events. Although snowfall events would lead to a significant temporary drop in blue ice fraction, the accumulated snow is often swept away by wind almost instantly in wind-induced blue ice

areas (Sinisalo and Moore, 2010), which leads to a high abundance and low variation of blue ice fraction.

The results in Fig. 4 indicate that the daily FABIAN product can be used to compute inter-annual variations of blue ice area extent. The resulting annual blue ice coverage variations are displayed in Fig. 5a over the entire ice sheet. The height of a single brick in a bar (i.e., an austral summer) stands for the area (in percentage of Antarctic continent) of pixels with a certain range of annual median blue ice fraction. The results show that pixels with annual median blue ice fraction $\geq 50\%$ through an austral summer is a potential indicator to qualify blue ice areas, as previously estimated from Hui et al. (2014) (1.67%) and Winther et al. (2001) (0.80% with a maximal potential extent to 1.60%). We also calculated the coefficient of variation of blue ice fraction for each 'brick' in Fig. 5a, shown in Fig. 5b, representing the temporal

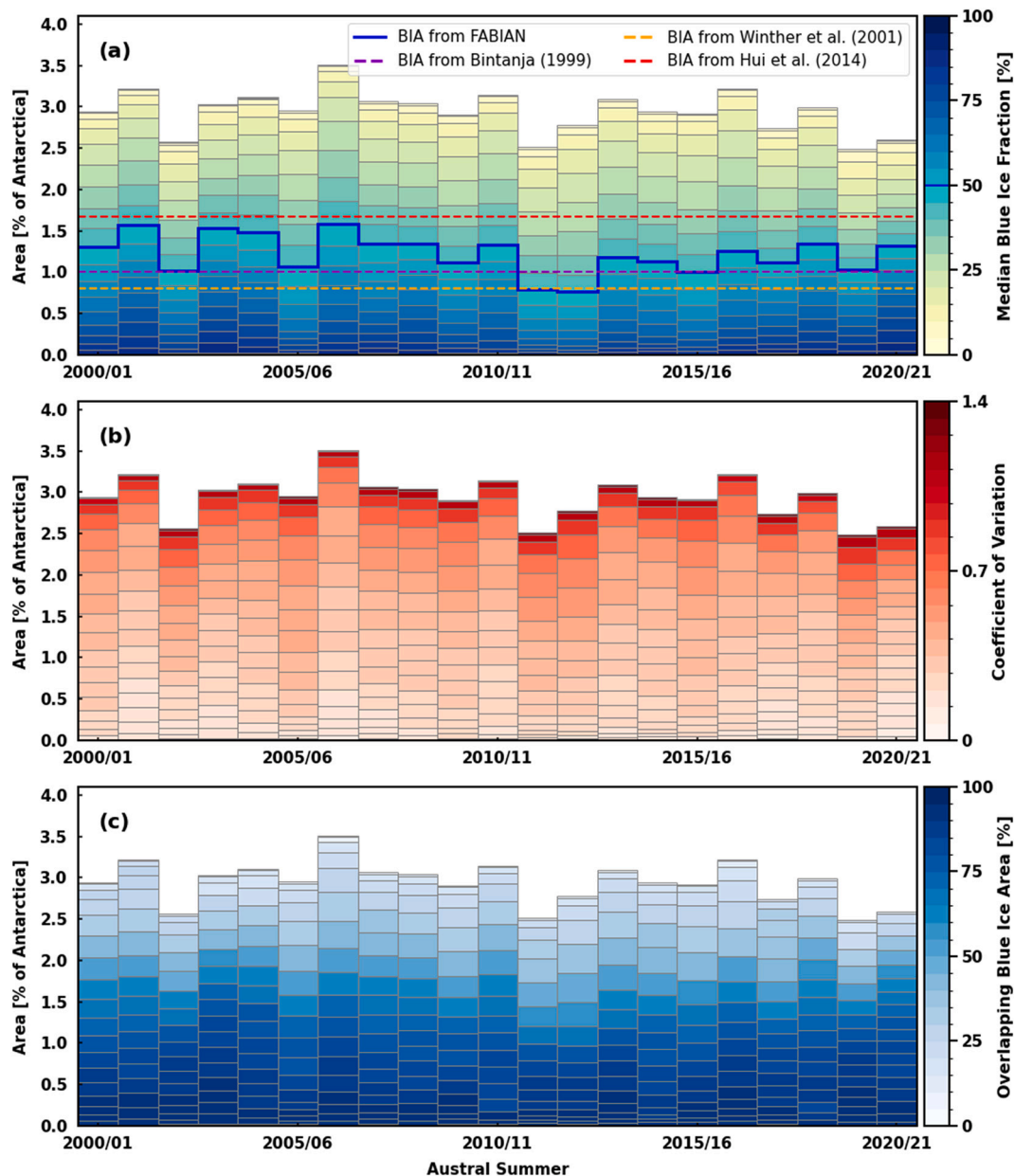


Fig. 5. Blue ice dynamics characterized by FABIAN (Fractional Austral-summer Blue Ice over Antarctica): (a) annual blue ice area (annual median blue ice fraction $\geq 50\%$) estimated by FABIAN, where the height of a single brick in a bar (i.e., an austral summer) stands for the area (in percentage of Antarctica) of pixels with a certain range of annual median blue ice fraction; (b) coefficient of variation concerning the blue ice fraction for each brick in subplot a; and (c) overlap areas between the pixels within a certain median blue ice fraction range and blue ice areas from Quantarctica (QANT-BIA) (Matsuoka et al., 2021) based on the Landsat image mosaic of Antarctica (LIMA) product (Bindschadler et al., 2008) using the Hui et al. (2014) method. (For interpretation of the references to colour in this figure legend, the reader is referred to the web version of this article.)

exposure of blue ice with different median blue ice fractions. Clearly, higher annual median blue ice fractions correspond to lower coefficients of variation. To geolocate these pixels with low blue ice fractions but high variations, we calculated the overlap areas between the pixels within a certain median blue ice fraction range and QANT-BIA. It confirms that areas with low annual median blue ice fractions are more likely to be temporally constraint melt streams, ponds/lakes, or the expanded melt-induced blue ice areas. In this context, we conclude that the median of annual blue ice fractions can be used as a proxy of blue ice occurrence. Together with the corresponding coefficient of variation results, median blue ice fractions hold a potential to separate wind-and melt-induced blue ice areas.

Still, FABIAN detects fewer blue ice areas than QANT-BIA (Fig. 4). There are several possible explanations: first, FABIAN agrees well with

the original results produced by Hui et al. (2014) (Fig. 3 in Hui et al., 2014), whereas QANT-BIA overestimates the blue ice fraction relative to Hui et al. (2014) and FABIAN. This seems to indicate that QANT-BIA lacks a snow grain size mask (Section 2.4), which is used in both our study and Hui et al. (2014). A second reason leading to the blue ice area disparities is the different spatial resolution between the MODIS and LIMA product. In this regard, some small patchy blue ice areas are omitted or only detected as very-low blue ice fraction areas in FABIAN.

3.2. Wind- vs. melt-induced blue ice

Apart from monitoring dynamics of blue ice areas at the continental scale with respect to their abundance and exposure, FABIAN is also able to characterize blue ice areas at the regional scale with respect to their

types. Wind-and melt-induced blue ice areas are formed by very different mechanisms, and their dynamics and anomalies express changes and variability of climatic drivers on different timescales. Zooming in to the regional scale, we demonstrate the ability of FABIAN to differentiate between wind-and melt-induced blue ice areas. A good example is the area of Lambert Glacier and Amery Ice Shelf, one of the most frequently studied blue ice areas. Previously, [Winther et al. \(2001\)](#) provided a blue ice area map differentiating between wind-and melt-induced blue ice areas based on prior knowledge and satellite observations. Using FABIAN, it is possible to investigate detailed spatiotemporal blue ice dynamics in both wind-and melt-induced blue ice areas, respectively.

As an example, we selected two blue ice areas located 480 km apart. The blue ice area near Goodspeed Nunataks ([Fig. 6](#), ~1600 m a.s.l.) is wind-induced, while the blue ice area near Gillock Island (~460 m a.s.l.) is melt-induced. Between 2000 and 2021, the RACMO2-estimated annual mean 2 m air temperature of the Goodspeed Nunataks blue ice area is -30.8°C , and the highest daily mean temperature in this period is -2.1°C . Surface melt therefore hardly occurs here. The blue ice area near Gillock Island has, on average, an annual surface melt of 87 mm w.e. per year, most of which in summer. The annual mean 2 m temperature is -19.7°C , and the daily mean can be as high as 3.3°C during summer.

The median blue ice fraction for the region of Lambert Glacier and Amery ice shelf is shown in [Fig. 6](#). The top subplots summarize the

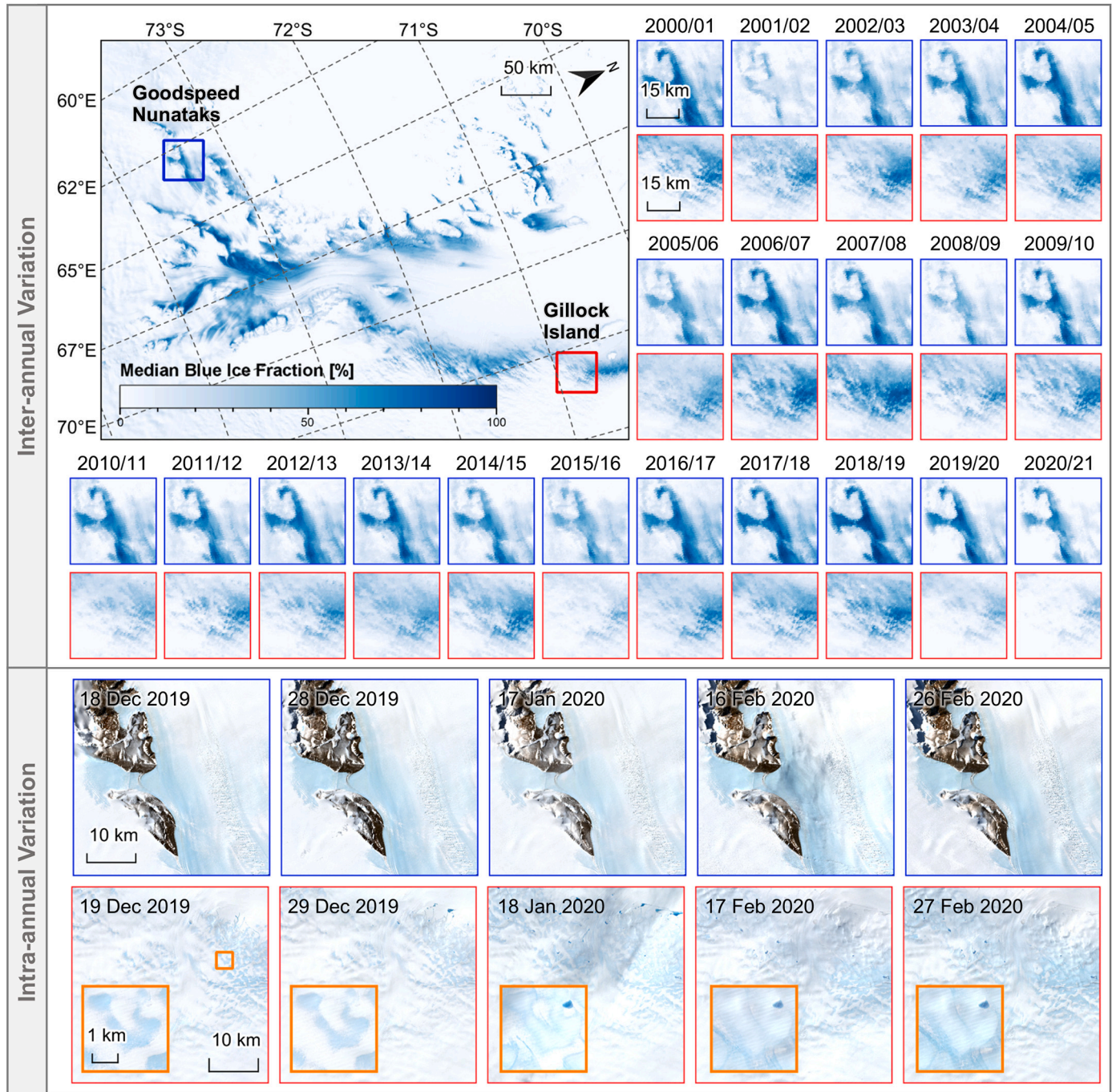


Fig. 6. Maps of overall median blue ice fraction over the Lambert Glacier adjacent to Amery Ice Shelf between austral summers 2000/01 and 2020/21, and its annual details near the Goodspeed Nunataks and Gillock Island (top). The subplots on the bottom are time series of (semi-) cloud-free Sentinel-2 images during the austral summer 2019/20. (For interpretation of the references to colour in this figure legend, the reader is referred to the web version of this article.)

median blue ice fractions for each austral summer between 2000/01 and 2020/21 near the Goodspeed Nunataks and Gillock Island. Generally, the blue ice area near the Goodspeed Nunataks has a higher annual median blue ice fraction than those near Gillock Island. Near the Goodspeed Nunataks, the pattern of high annual median blue ice fraction ($>50\%$) is consistently present in all austral summers between 2000/01 and 2020/21, except for 2001/02. In that exceptional year, seasonal snow very likely concealed those blue ice areas. Although snow is often blown off of wind-induced blue ice areas, patchy snow can sometimes persist for weeks or even years (Sinisalo and Moore, 2010). In Gillock Island, there are no areas with consistently high annual median blue ice fractions.

Intra-annual variations are summarized in the bottom subplots for the austral summer 2019/20 based on (semi-) cloud-free Sentinel-2 observations. It clearly illustrates that the blue ice areas near the Goodspeed Nunataks are invariant during the austral summer, and no melting features (streams, ponds/lakes) have been observed. Yet, the development of melt ponds/lakes is clearly observed near Gillock Island, and that blue ice was expanding throughout the austral summer.

3.3. Blue ice variability and meteorological conditions

FABIAN is based on daily observations, instead of a static mosaic. Thus, FABIAN can be combined with daily output of meteorological variables from (regional) climate models in order to explain the dynamics and appearance of blue ice in terms of the surface meteorology. Blue ice fraction fluctuates from year to year, and in this section, we relate these variations to surface meteorological conditions. To this end, we use 2 m temperature, snowfall, wind speed, surface melt, and sublimation retrieved from the regional climate model RACMO version 2.3p2 (Van Wessem et al., 2018), RACMO2 henceforth. Time series for wind-induced blue ice areas (near the Goodspeed Nunataks in Fig. 7) and melt-induced blue ice areas (in Gillock Island in Fig. 8) are shown for the sub-period 2011/12–2018/19, for a better visualization. In the wind-induced blue ice area (Fig. 7), RACMO2 simulates no surface melt but sublimation instead, fitting the definition given by Bintanja (1999). The lower blue ice fraction in the austral summer 2015/16 coincides with a period of low wind speed at the start of that season in RACMO2. It could mean that winter snowfall was able to accumulate for a longer period. Within a single austral summer, changes in wind patterns also lead to blue ice fraction anomalies without significant snowfall (purple

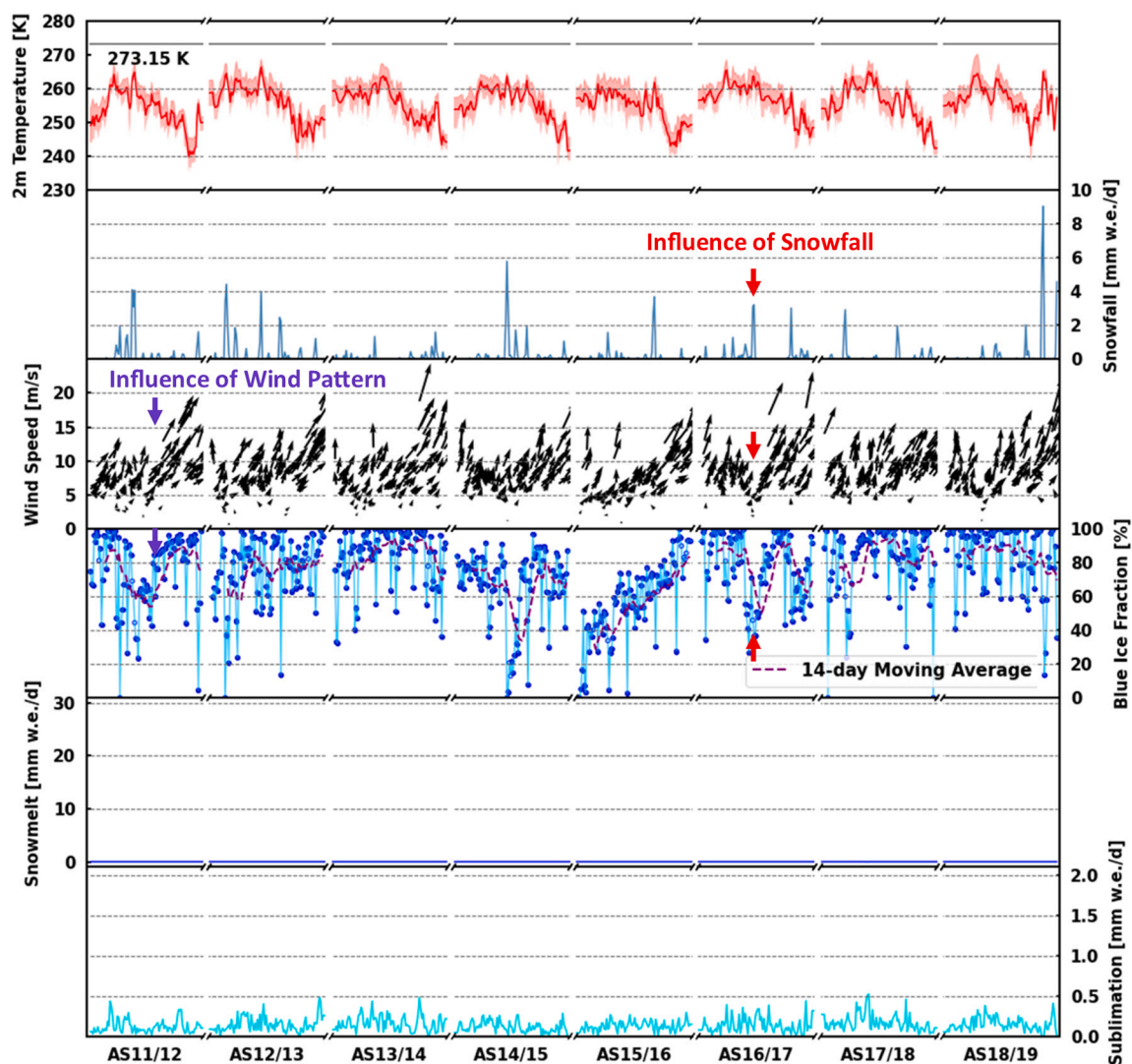


Fig. 7. Blue ice fraction during austral summers (ASs) derived from FABIAN (Fractional Austral-summer Blue Ice over Antarctica) and contemporaneous meteorological conditions derived from the regional atmospheric climate model RACMO2 (Van Wessem et al., 2018) at a wind-induced blue ice location (73.40°S, 62.40°E) near the Goodspeed Nunataks. The solid red line represents the daily mean 2 m temperature, and the red area stands for the range between the maximum and minimum of daily 2 m temperature. (For interpretation of the references to colour in this figure legend, the reader is referred to the web version of this article.)

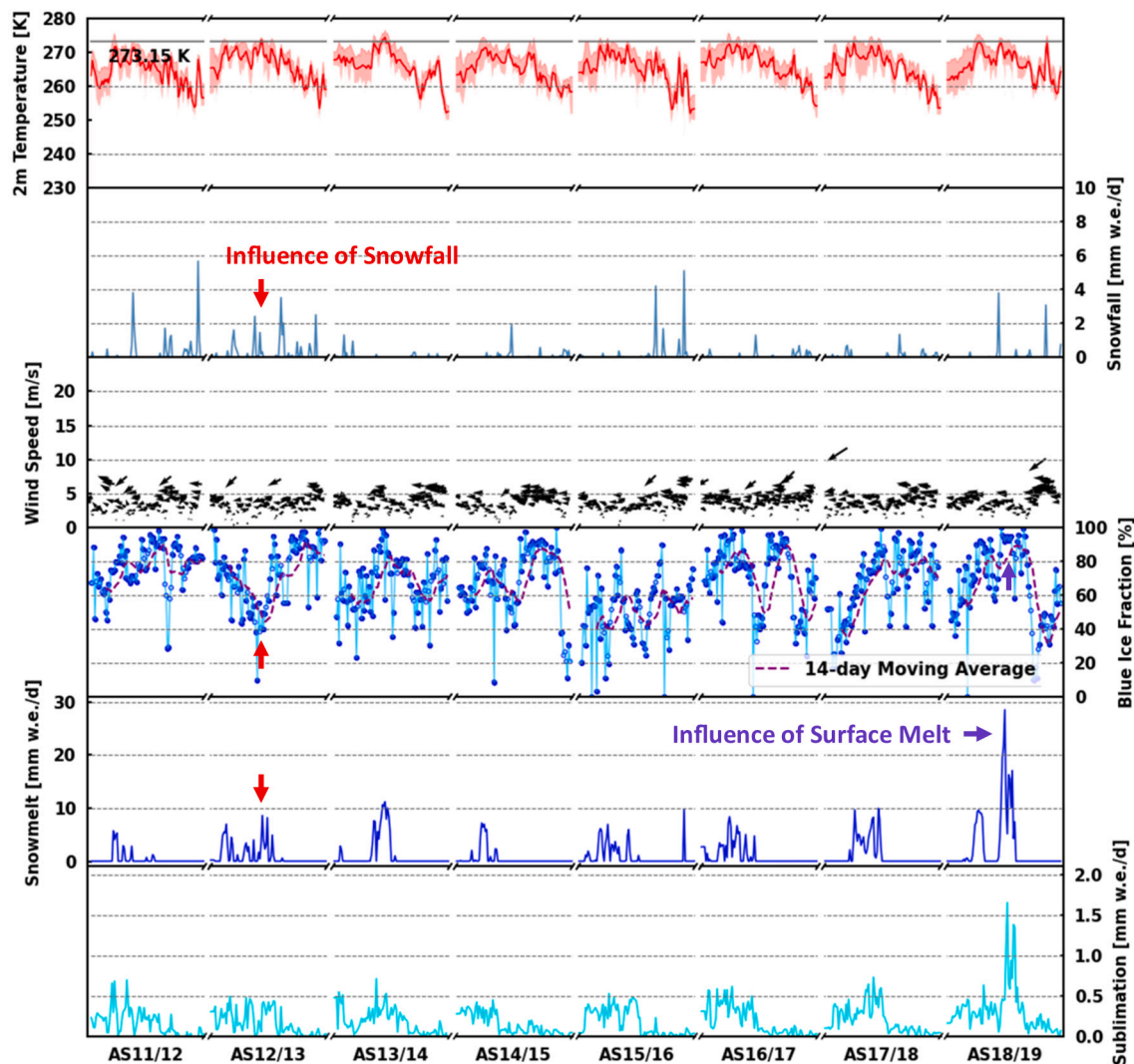


Fig. 8. Blue ice fraction during austral summers (ASs) derived from FABIAN (Fractional Austral-summer Blue Ice over ANtarcctica) and contemporaneous meteorological conditions derived from the regional atmospheric climate model RACMO2 (Van Wessem et al., 2018) at a melt-induced blue ice location (70.55°S, 72.96°E) in Gillock Island. The solid red line represents the daily mean 2 m temperature, and the red area stands for the range between the maximum and minimum of daily 2 m temperature. (For interpretation of the references to colour in this figure legend, the reader is referred to the web version of this article.)

arrows in Fig. 7). Such areal changes in wind-induced blue ice areas have been explained previously by altered wind circulation (Bintanja and Van den Broeke, 1995a, 1995b; Brown and Scambos, 2004). Also, a high-snowfall event (indicated with red arrows in Fig. 7) can temporarily reduce the blue ice fraction, shown as a very sharp drop (more than 50%). Often, these reductions in blue ice area extent do not last long, because the relatively strong winds normally erode the snow quickly (Sinisalo and Moore, 2010). However, in the melt-induced blue ice areas, the wind speed is lower than in the wind-induced blue ice areas (Fig. 8). It also reveals the major difference between wind- and melt-induced blue ice areas formation, according to their definitions (Winther et al., 2001; Bintanja, 1999).

In the melt-induced blue ice area of Gillock Island in most years, there is a seasonal cycle of blue ice fraction, with a maximum occurring around the middle of austral summer. It can be explained by the seasonal cycle in temperature (Fig. 8) and the related occurrence of surface melt. The timing of high blue ice fraction agrees with the occurrence of surface melt and coincidence with the periods with high 2 m temperature. Sublimation also has a stronger seasonal cycle in the melt-induced blue ice area, because of the nonlinear dependency of saturated water vapor

pressure on temperature and the strong variation in surface type throughout the season. Blue ice has a lower albedo (0.56) than snow (0.80) (Bintanja and Van den Broeke, 1995a, 1995b), it absorbs more solar radiation than snow, which amplifies its sublimation rate during summer (Bintanja and Van den Broeke, 1995a, 1995b). Similar to wind-induced areas, snowfall (including its magnitude and lasting period) is the most direct factor influencing the daily blue ice fraction in melt-induced blue ice areas. Unlike the quick recovery of blue ice fraction in wind-induced blue ice areas, blue ice fraction in melt-induced blue ice areas tends to rise more slowly with the melt of the snowpack. Likewise, snow is harder to remove once it has melted, resulting in less efficiently removed by increased wind to erode the accumulated snow (red arrows in Fig. 7). Winds are also considerably weathered away from the katabatic wind zone in the escarpment. In this manner, daily blue ice fraction time series vary smoother in melt-induced blue ice areas than those in wind-induced blue ice areas.

Due to similar spectral properties, differentiating between wind- and melt-induced blue ice areas is challenging solely based on satellite images (Winther et al., 2001). However, FABIAN opens up the possibility to make the distinction based on the temporal signature of blue ice

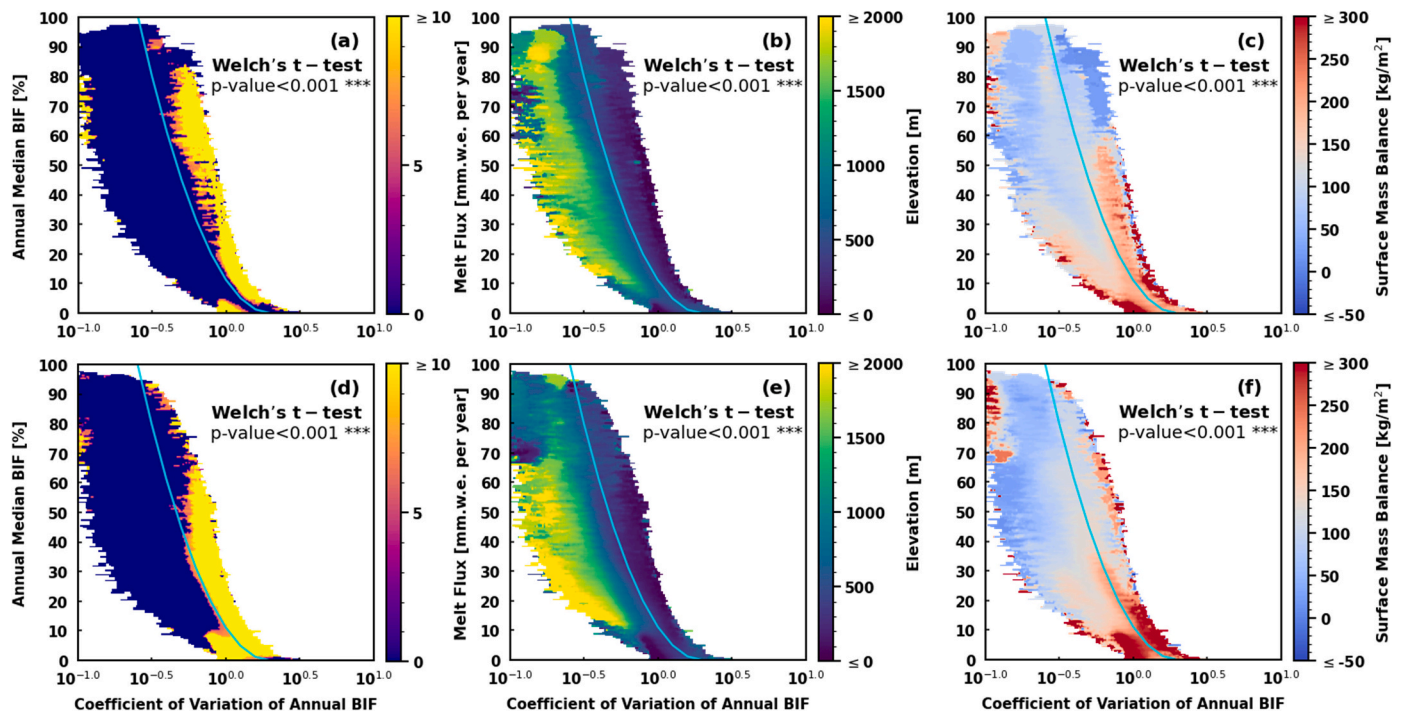


Fig. 9. Binned scatter plots illustrating intra-annual dynamics of Antarctic blue ice fraction (BIF) over the full Antarctic continent for two summers with a low BIF (2002/03, shown in a–c) and a high BIF (2006/07, shown in d–f), identified in Fig. 5a, coloured according to the median of annual melt flux, elevation, and annual surface mass balance. The melt flux (Trusel et al., 2013) is derived from the QuikSCAT (Quick Scatterometer), elevation information is obtained from the TanDEM-X 90 m digital elevation model (Rizzoli et al., 2017), and surface mass balance is simulated by the regional atmospheric climate model RACMO2 (Van Wessem et al., 2018). The cyan line is a quadratic function separating potential wind- and melt-induced blue ice areas: $y = 0.0125(100x - 130)^2$, where y is annual median BIF, and x is the coefficient of variation of annual BIF. (For interpretation of the references to colour in this figure legend, the reader is referred to the web version of this article.)

fraction, which is a unique advantage of our FABIAN to previous mosaic-based and mono-temporal blue ice products on an annual basis. We illustrate the potential separation into wind- and melt-induced blue ice areas based on the annual median blue ice fraction and coefficient of variation of annual blue ice fraction for each pixel, applied over the full Antarctic continent. Fig. 9 shows the results for blue ice fraction over the full Antarctic continent for two austral summers with a low blue ice fraction (2002/03, shown in a–c) and a high blue ice fraction (2006/07, shown in d–f), identified in Fig. 5a. As a general pattern, blue ice with a high annual median blue ice fraction has a low coefficient of variation, and vice versa. In panels a and d of Fig. 9, we colour-code the feature space by surface melt flux from Trusel et al. (2013). For the same value of annual median blue ice fraction, pixels with surface melt are of higher coefficients of variation, which indicates the melt-induced blue ice areas are more variable in time than wind-induced blue ice areas. When colour-coding by elevation (Fig. 9b and e), pixels with the same annual median blue ice fraction level, have a higher coefficient of variation at lower elevation. It confirms that melt-induced blue ice areas, which are located at lower elevation, are more variable than wind-induced blue ice areas (Winther, 1994; Liston et al., 1999). Finally, when colour-coded according to RACMO2 surface mass balance, blue ice areas with negative surface mass balances correspond to zero surface melt, located at high elevation zones. It agrees with the definition of wind-induced blue areas of negative surface mass balance by van den Broeke et al. (2006). A quadratic function (cyan lines in Fig. 9) can be used to approximate a distinction between the blue ice area types. This quadratic function can statistically-significantly (p -values < 0.001 with Welch's t -test) separate samples of variables (i.e., melt flux, elevation, and surface mass balance) from the left and right of the quadratic function. Along these lines, a further refined distinction between wind- and melt-induced blue ice areas can be developed.

3.4. Complex surface types in melt-induced blue ice areas

Strictly speaking, 'melt-induced blue ice areas' are not pure bare ice surfaces but showing a blue-ice-appearance/spectrum, since they also include slush, melt streams, and shallow supraglacial lakes. It is not only by its definition (Winther et al., 2001), but also in FABIAN due to our endmember selection, and pooling of slush and blue ice into one single 'blue-ice' surface type. However, perfectly distinguishing between wind- and melt-induced blue ice areas using optical imagery is mainly challenged by their spectral similarity under the presence/concentration of ice-bound snow crystals, encapsulated air bubbles, and debris Winther et al. (2001). At an annual scale, FABIAN holds a potential to separate these two blue ice types (Section 3.1). However, at a daily basis, its indication and uncertainty, particularly regarding melt-induced blue ice areas, still need to be evaluated.

In this section, we take as an example a time series of a melt-refreezing cycle of a supraglacial lake (the entire supraglacial lake including (partially) frozen one illustrated in Fig. 10) evolving over a blue ice area at Amery Ice Shelf during austral summer 2019/20 based on FABIAN, cloud-free Sentinel-2 images, Sentinel-2-derived blue ice area maps (based on the method in Section 2.5), and Sentinel-2-derived supraglacial lake maps (Dirscherl et al., 2021) (Fig. 10). It is a supraglacial lake of which the northern part is open water, and its southern part consists of frozen lakes surrounded by melt streams. At the beginning of the ablation season, Sentinel-2 shows that both the north and south parts are partially classified as blue ice areas. FABIAN indicates a low blue ice fraction, but an increasing wet snow fraction, which indicates the melting of the snow layer above the supraglacial lake. In the middle of the ablation season, the south part of the supraglacial lake turns into open water. Accordingly, the extent of Sentinel-2-based blue ice areas shrinks. FABIAN indicates an increase in both blue ice fraction

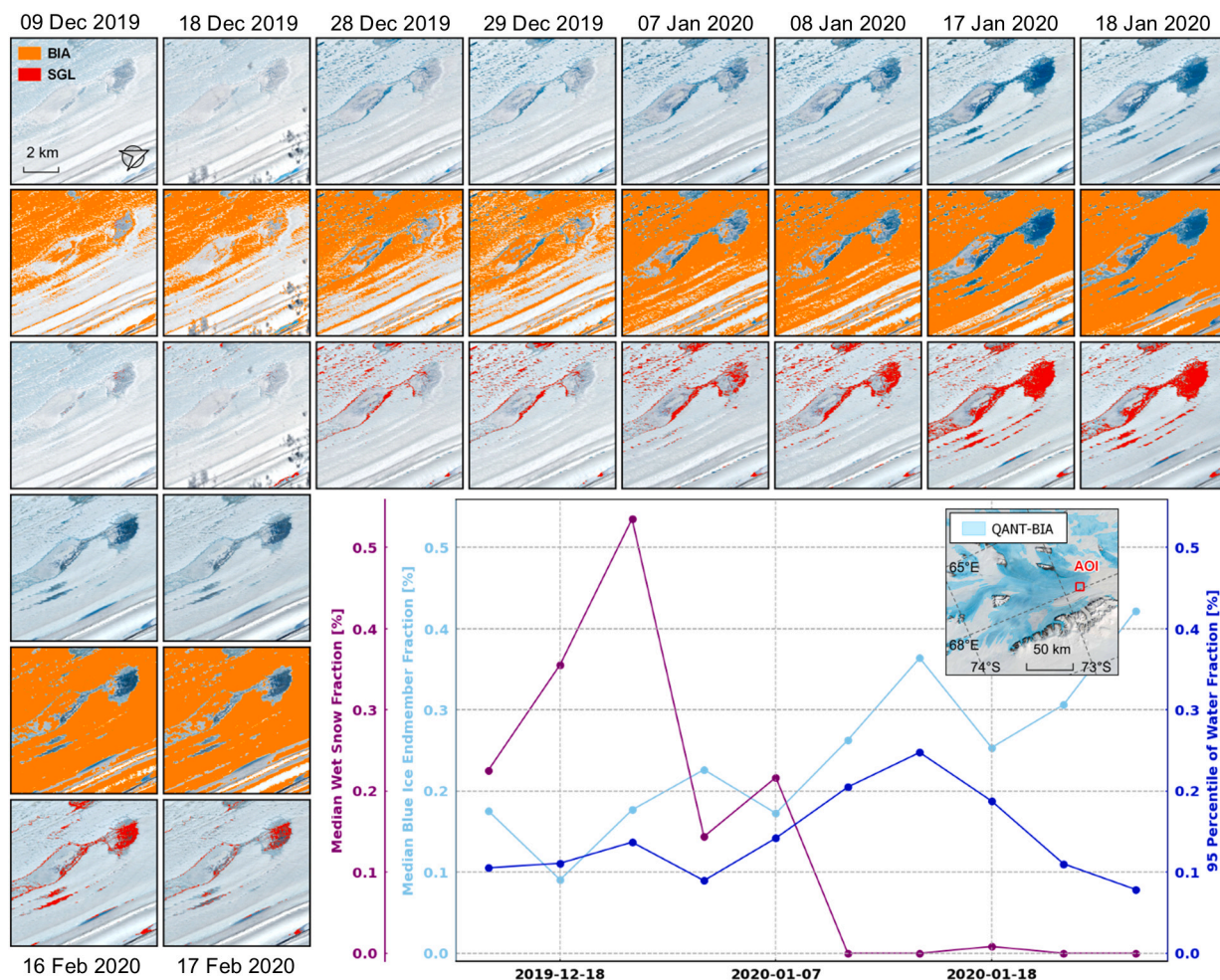


Fig. 10. Dynamics of blue ice, wet snow, and a supraglacial lake (SGL) evolving over a blue ice area (BIA) at Amery Ice Shelf during austral summer 2019/20. The satellite images, blue ice areas, and supraglacial lake extents (Dirscherl et al., 2021) are derived from Sentinel-2, and the endmember fractions in the time series plot are derived from FABIAN (Fractional Austral-summer Blue Ice over Antarctica). The blue ice area extent shown in the overview map of the line-plot is derived from Quantarctica (QANT-BIA) (Matsuoka et al., 2021) based on the LIMA product (Bindschadler et al., 2008) using the Hui et al. (2014) method. (For interpretation of the references to colour in this figure legend, the reader is referred to the web version of this article.)

and water fraction. Near the end of the ablation season, when the supraglacial lake starts to refreeze, Sentinel-2 classifies the southern refrozen part as blue ice area. FABIAN continues to indicate a decrease in water fraction and zero wet snow fraction, instead the blue ice fraction continues to increase which is likely due to slush or shallow refrozen ponds/lakes.

Although FABIAN captures the overall dynamics of wet snow, blue ice, and water, there is on average a $\sim 56\%$ underestimation of blue ice areal extent when compared to Sentinel-2-based blue ice area. We suspect that wet snow and water contaminate our estimate of blue ice fraction in melt-induced blue ice areas, especially in outlet glaciers. To investigate this in more detail, we have compared Sentinel-2 blue ice area with different FABIAN surface type mixtures: (1) the original blue ice fraction, (2) the FABIAN blue ice fraction adding the wet snow fraction, (3) FABIAN blue ice fraction adding the water fraction, and (4) FABIAN-derived blue ice fraction adding both the wet snow fraction and water fraction. The median $RMSE_{SMA}$ between Sentinel-2 and each of these four FABIAN settings are summarized in Table 2 and shown as maps in Fig. C.15. In wind-induced blue ice areas, $RMSE_{SMA}$ is at most slightly improved (mostly $< 1\%$) when additional surface types are added, or it even deteriorated like in Victoria Land (AOI 6). In contrast, obvious improvements ($\sim 3\%$) are found in melt-induced blue ice areas like Lambert Glacier (AOI 4). It suggests that the blue ice fraction is

partially calculated as other endmember fractions that are similar to blue ice.

3.5. Sentinel-2 accuracy and cloud cover

We use Sentinel-2 high-resolution maps as a benchmark to validate FABIAN at the coarser spatial scale of MODIS. In contrast to previous studies (Winther et al., 2001; Hui et al., 2014), we used individual Sentinel-2 images instead of cloud-free mosaics. In these images, clouds,

Table 2

The root mean square error (RMSE in %) of spectral mixture analysis (SMA) in estimating blue ice fraction (BIF) or combined with wet snow fraction (WSF) and/or water fraction (WAF), compared to the Sentinel-2 observations during the austral summer 2018/19 to 2020/21 in each area of interest (AOI). Bold numbers indicate the lowest RMSE values in a certain AOI.

	BIF	BIF + WSF	BIF + WAF	BIF + WSF + WAF
AOI 1	30.43	29.86	30.10	29.68
AOI 2	28.36	27.97	28.05	27.94
AOI 3	26.18	26.64	25.47	26.22
AOI 4	37.09	34.84	36.12	34.48
AOI 5	35.11	35.23	33.96	34.54
AOI 6	24.70	31.80	25.55	34.10

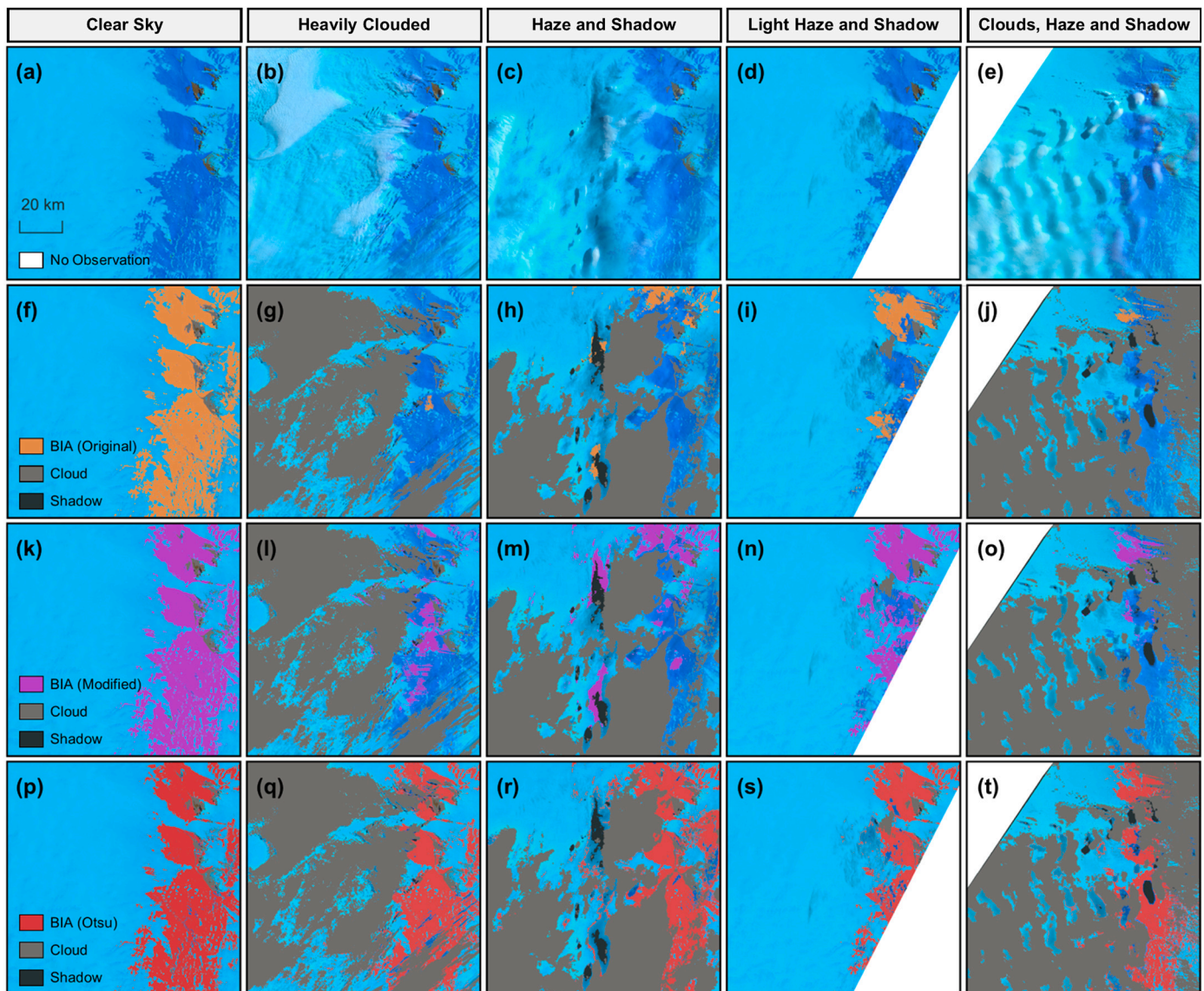


Fig. 11. Results of the blue ice area classification near the Queen Fabiola Mountains (AOI3) based on Sentinel-2 images in false-colour (R: band 12, G: band 8A, B: band 3) combination (a–e) using the Hui et al. (2014) method with the originally fixed threshold (0.90, f–j), modified threshold (0.85, k–o), and dynamic threshold using the Otsu method (p–t) under different cloudy conditions: cloud-free (a, f, k, p), heavily cloudy (b, g, i, q), heavily hazy with snow in cast shadow (c, h, m, r), lightly hazy with snow in cast shadow (d, i, n, s), cloudy and hazy with snow and blue ice area in cast shadow (e, j, o, t). (For interpretation of the references to colour in this figure legend, the reader is referred to the web version of this article.)

haze and cloud shadow are not always fully detected by the applied cloud and shadow mask (Fig. A.14). In this section, we explore the performance of the blue-ice classifiers under different cloud conditions, including haze and shadow. In cloud-free conditions, all three classifiers show similar blue ice classifications (Fig. 11). When it becomes cloudy, the three classifiers start to differ strongly. We discover a *phantom blue ice area* phenomenon, i.e., an overestimation in blue ice area in regions with snow in cast shadow, particularly in the results from the modified classifier (Fig. 11h, m–n). It has also been found in blue ice area maps produced using the Otsu method, but only in (illuminated) shadow/haze

boundaries (Fig. 11r–s). This is due to the spectral mixture of (fresh and coarse-grained) snow, shadow and thin haze, resulting in a blue-ice-like spectrum which confuses the applied blue ice area classifier. Also, an underestimation of blue ice areas under haze is shown in blue ice area maps using the original (Fig. 11g–j) and modified (Fig. 11i–o) classifier, i.e., thresholding based on a fixed global value. Occasionally, it also occurs in blue ice area maps (Fig. 11r–t) produced using dynamic thresholding (i.e., the Otsu method), but over a relatively smaller area. This is partially the result of undetected clouds and haze, but also due to an inaccurate atmospheric correction, leading to distortions in the

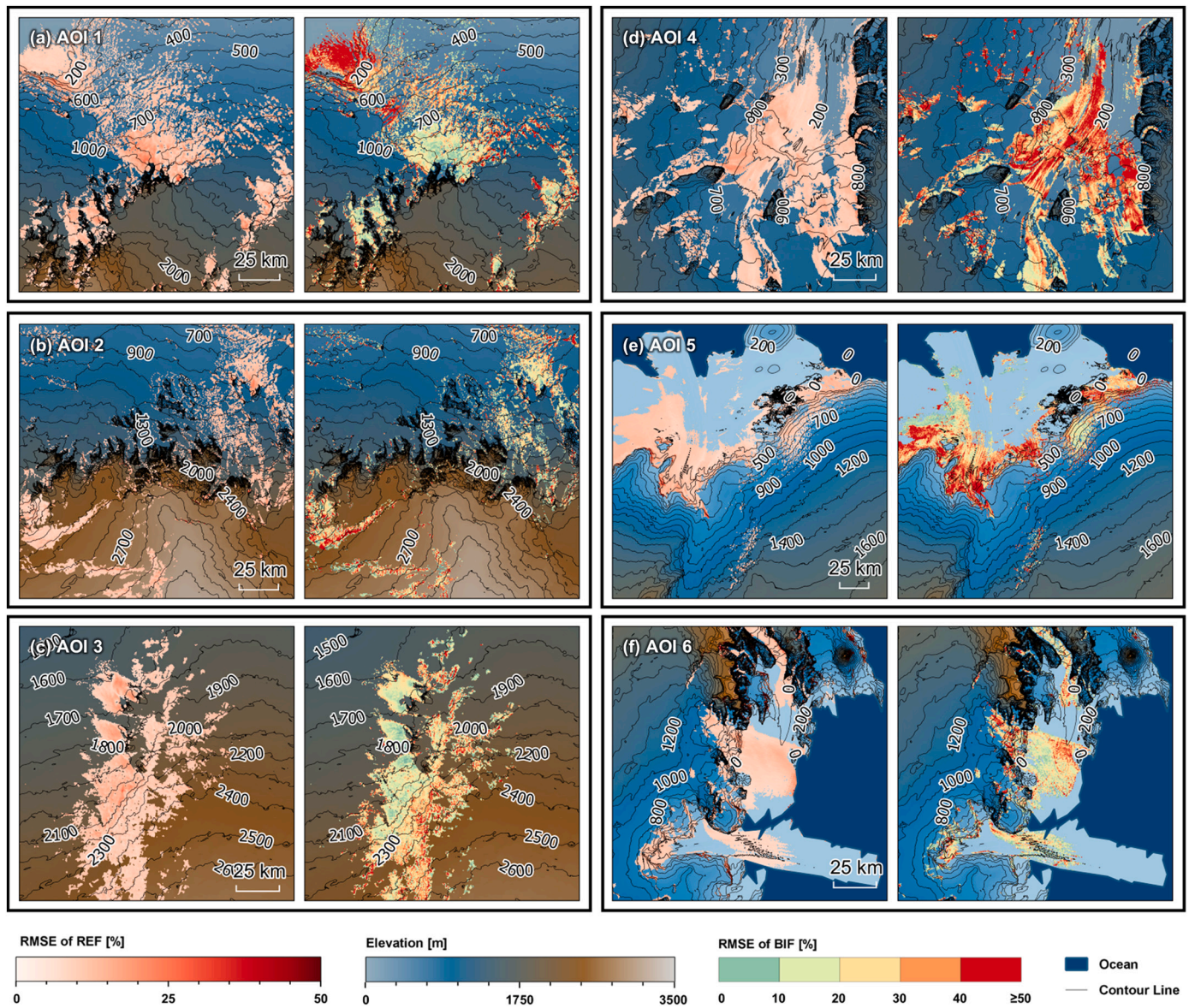


Fig. 12. Overview of the root mean square error of spectral mixture analysis (SMA) in modeling the observed surface reflectance ($RMSE_{REF}$) during the austral summer 2000/01 to 2020/21, the root mean square error of SMA in estimating blue ice fractions ($RMSE_{BIF}$) compared to the Sentinel-2 observations during austral summer 2018/19 to 2020/21 in each area of interest (AOI): (a) the Petermann Ranges, (b) Sør-Rondane Mountains, (c) Queen Fabiola Mountains, (d) Amery Ice Shelf, (e) Shackleton Ice Shelf, and (f) Victoria Land. (For interpretation of the references to colour in this figure legend, the reader is referred to the web version of this article.)

spectral profiles. Detailed quantitative comparison of results from different classifiers can be found in [Appendix D](#). Although the Otsu-classified blue ice areas provide the best results, the aforementioned over-/under-estimations in blue ice area (due to undetected clouds, haze, and their shadow) can still propagate to the blue ice area-aggregated blue ice fraction. Thus, attention is needed when comparing blue ice area-aggregated blue ice fraction with SMA-estimated blue ice fraction.

3.6. Uncertainty in spectral mixture analysis (SMA)

The performance of SMA in modeling the observed surface reflectance and blue ice fraction is displayed in [Fig. 12](#). The applied SMA does not show an obvious spatial pattern in $RMSE_{REF}$, indicating that there are no crucial endmembers missing. The area with the highest $RMSE_{REF}$ is Victoria Land (AOI 6), especially in areas with sea-ice and mountains, where the selected rock and deep water endmembers are not sufficiently representative. In the remaining areas, the $RMSE_{REF}$ values are also high, particularly in the areas with steep slopes, especially at the foot of the mountains. Since the surrounding high-elevation terrain casts shadow

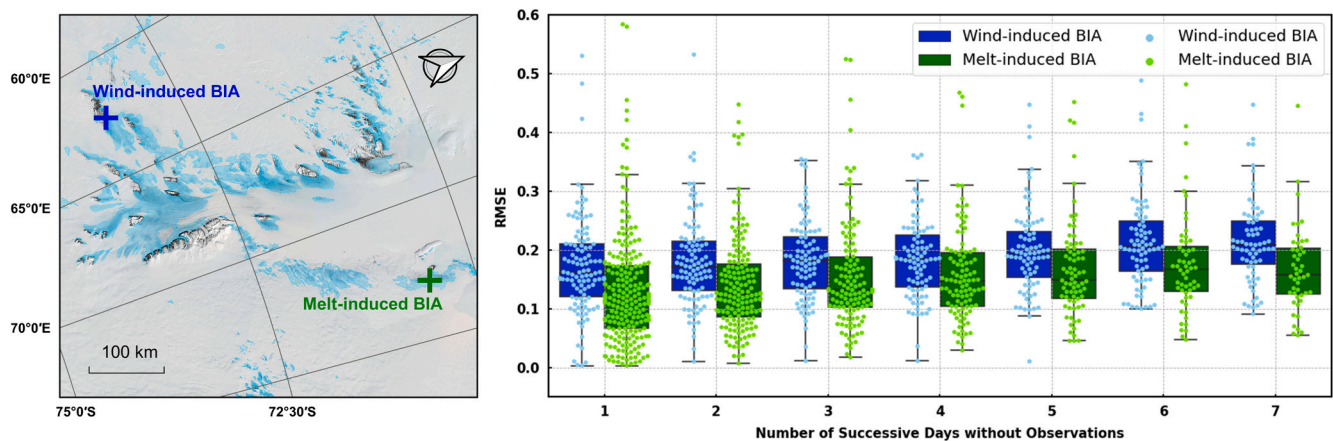


Fig. 13. The root mean square error (RMSE) based on leave- n -out ($1 \leq n \leq 7$) cross-validation of two selected demonstrative wind-induced (near the Goodspeed Nunataks; blue cross at 73.93°S, 66.80°E) and melt-induced (in Gillock Island; green cross at 70.55°S, 72.96°E) blue ice areas (BIAs). (For interpretation of the references to colour in this figure legend, the reader is referred to the web version of this article.)

on these areas, their spectra are contaminated by shadow, resulting in high $RMSE_{REF}$ values. Perhaps, this effect could have been mitigated by including a shadow endmember in the SMA. But as we think the shadow endmember is the least crucial, we did not select it in our study.

The validation based on the contemporaneous Sentinel-2-derived blue ice fraction is summarized in Fig. 12, and previously in Table 2. In general, the median RMSE ranges from 24.7% to 37.1%. The spatial pattern shows that $RMSE_{SMA}$ is significantly lower (around 10% ~ 20%) over wind-induced blue ice areas than in melt-induced blue ice areas (around 20% ~ 30%). Over bare ice, $RMSE_{SMA}$ can increase to 40%, e.g., over Amery Ice Shelf and Shackleton Ice Shelf. It is seemingly linked to the representativeness of blue ice endmembers. In wind-induced blue ice areas, blue ice is quite uniform in its appearance, while melt-induced blue ice shows strong variations in surface type and appearance, including ice, slush, shallow melt streams and lakes. This transition was pointed out by Winther et al. (2001): when liquid water is present in melt-induced blue ice areas, the reduction of reflectance can lead to the confusion between wind- and melt-induced blue ice. Such cases occur very likely over bare ice and at edges of wind-induced blue ice areas. Depending on the status of the blue ice area, the real-time blue ice area spectrum might not be a linear mixture of the selected endmembers. It is worth mentioning that there is uncertainty also in Sentinel-2-derived blue ice areas (Section 3.5), which can propagate to the blue ice fraction results. By manual inspection, we find that $RMSE_{SMA}$ is higher especially in the melt-induced blue ice areas.

3.7. Uncertainty from gap-filling

In order to produce a daily blue ice fraction from MODIS data, we had to fill data gaps due to clouds and missing data. This produces an uncertainty, which is likely to become larger as the length of the data gap increases. The median number of successive days without valid MODIS observations for austral summers 2000/01 to 2020/21 is summarized in Fig. 3 on a pixel basis. After combining Terra and Aqua observations, the probability of MODIS cloudiness is less than 20% in

Antarctic blue ice areas. Data gap length is higher in coastal Antarctica than in the interior of the ice sheet, and especially high in mountainous areas such as the Antarctica Peninsula, Amery Ice Shelf, and coastal Dronning Maud Land. In blue ice areas, the median data gap is less than one week. In this study, we masked out cloud pixels in MODIS imagery according to the '1 km Reflectance Data State' band. It is produced by the MODIS cloud mask algorithm (Baum et al., 2012; Frey et al., 2008; Ackerman et al., 1998), and its overall accuracy were reported better than 85% compared with ground LiDAR (light detection and ranging) observations (Frey et al., 2020; Ackerman et al., 2008). For local studies, additional attentions should also be paid to the under- and over-detection of cloud pixels, which can affect not only the accuracy of the retrieved blue ice fraction, but also the length of data gap.

To assess the uncertainty associated with gap-filling, we performed a leave- n -out ($1 \leq n \leq 7$) cross-validation, in which we purposely left out one to seven consecutive days of data (Fig. 13) in all available time-series with a number of $\geq n + 2$ consecutive valid observations. The median RMSE of the interpolation is around 15%, increasing slightly along with the number of successive days without valid observations. The RMSE range between lower and upper quantile is lower in melt-induced blue ice areas than in wind-induced blue ice areas, particularly when the period without successive observations increases. This is in line with the dynamics of blue ice areas presented in Section 3.3. In wind-induced blue ice areas, snowfall events lead to very sharp (more than 50% per day) but brief (recovered often within two days) drops in blue ice fraction, and the accumulated snow is often swept away by strong winds, resulting in a quick recovery of the blue ice fraction. In seasonal blue ice areas however, the dynamics of daily blue ice fraction is cyclical and more gradual in time, suggesting that the variation of blue ice fraction during a short period of interpolation is less than the steep drop and climb in wind-induced blue ice areas. The RMSE range between lower and upper quantile decreases with the increases of successive days without valid observations in melt-induced blue ice areas, but not in wind-induced blue ice areas. As illustrated in Fig. 7, given the nature of wind-induced blue ice areas, where the accumulated fresh

snow is often quickly swept away, the corresponding blue ice fraction is often increased within few days. If clouds are still there (missing data), this increase will be averaged through the cloudy period, resulting in a high RMSE. While in the melt-induced blue ice areas, the increase of blue ice fraction is much slower due to melt presence. Such a gradual increase of blue ice fraction is less dependent on number of cloudy days (i.e., missing data), resulting in a lower RMSE.

4. Conclusions

In this study, FABIAN is presented, which is a daily product of blue ice fraction over Antarctica covering the austral summers from 2000/01 to 2020/21. FABIAN estimates daily blue ice fraction using spectral mixture analysis (SMA) performed on moderate resolution imaging spectroradiometer (MODIS) observations in Google Earth Engine. The input spectra are measured in lab or field campaigns, observed by MODIS, and simulated using a physical model. After a careful end-member selection, the applied linear SMA accurately estimates the observed MODIS reflectance without a significant spatial pattern in the corresponding root mean square error images in blue ice areas, suggesting that the endmember selection for blue ice areas was appropriate. Based on blue ice fractions aggregated from higher-resolution blue ice area maps derived from contemporaneous Sentinel-2 images, FABIAN-derived blue ice fractions agree better in wind-induced blue ice areas (median $RMSE_{BIF}$ between 10% and 20%) than in melt-induced blue ice areas (median $RMSE_{BIF}$ between 20% and 30%) across the six selected test sites in coastal East Antarctica. To fill the original data gaps in MODIS observations, weekly and monthly mean values are used. According to a leave- n -out ($1 \leq n \leq 7$) cross-validation, the median RMSE produced by this interpolation is around 15%.

FABIAN demonstrates its capacity to identify blue ice areas, and the intra- and inter-annual pattern of blue ice fraction variation at a continental and regional scale. Together with the regional climate model RACMO2, FABIAN reveals blue ice dynamics under the influence of air temperature, wind, and snowfall, which are in line with previous studies based solely on model simulations. So far, the main challenge for

FABIAN in accurately estimating blue ice fraction is dealing with wet snow, slush or shallow melt ponds/lakes, as their spectral profiles can be similar to the blue ice spectrum in MODIS bands. As a direction for future research and refinement, we suggest that endmember selection could be further optimized at a pixel scale (e.g., using multiple end-member spectral mixture analysis, MESMA (Roberts et al., 1998)), and/or that the set of endmember candidates could be further extended with high-quality spectra measured in situ in Antarctica.

CRedit authorship contribution statement

Zhongyang Hu: Conceptualization, Methodology, Software, Formal analysis, Writing – original draft, Visualization. **Peter Kuipers Munneke:** Conceptualization, Methodology, Investigation, Writing – original draft, Supervision, Visualization. **Stef Lhermitte:** Conceptualization, Methodology, Formal analysis, Writing – review & editing, Supervision. **Mariel Dirscherl:** Resources, Investigation, Writing – review & editing. **Chaonan Ji:** Visualization, Writing – review & editing. **Michiel van den Broeke:** Investigation, Writing – review & editing, Supervision.

Declaration of Competing Interest

The authors declare that they have no known competing financial interests or personal relationships that could have appeared to influence the work reported in this paper.

Data availability

Data will be made available on request.

Acknowledgement

The authors would like to thank Dr. Ghislain Picard, Dr. Steve Warren, Dr. Fengming Hui, and Dr. Maria Zatko for providing modeled wet snow spectrum and in-situ spectra measurements. This research was funded by the Netherlands Space Office (NSO) grant ALWGO.2018.039.

Appendix A. Cloud Masks

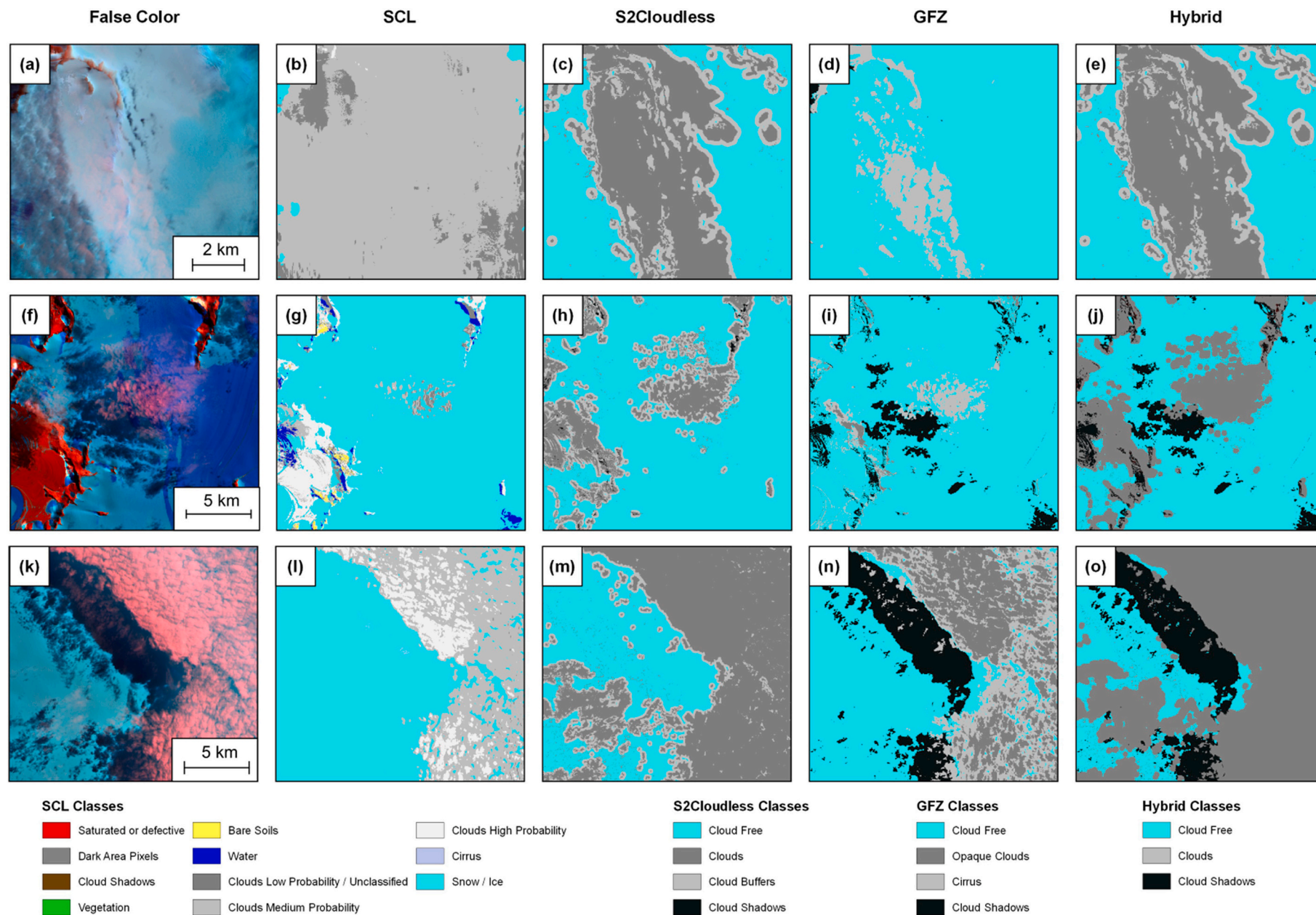


Fig. A.14. Cloud masks for Sentinel-2 imagery based on the scene classification map (SCL), s2cloudless, GFZ method, and hybrid method, under different cloudiness: hazy (a-e), partially cloudy/hazy (f-j), heavily cloudy (k-o).

Appendix B. Automatic endmember (AUTO-EM) generator for endmember derivation

Table B.3

Classification methods applied in the automatic endmember (AUTO-EM) generator for endmember derivation from the moderate-resolution imaging spectroradiometer (MODIS) imagery.

Endmember	Thresholds	References
Blue ice	$0.90 < BR_{47}$ $0.30 < \rho_{NIR} < 0.70$ $0.85 < \rho_{blue}^*$	(Hui et al., 2014)
Bare Rock	$NDSI < 0.75$	(Burton-Johnson et al., 2016)
Slush	$0.25 < \rho_{SWIR}$ $0.12 < NDWI_{ICE} < 0.14$	(Bell et al., 2017; Zatko and Warren, 2015; Yang and Smith, 2012)
Water	$0.40 < \rho_{blue}$ $0.25 < NDWI_{ICE} < 0.45$ $\rho_{blue} < 0.2$	(Bell et al., 2017; Yang and Smith, 2012; Burton-Johnson et al., 2016)

* Indicates where the original threshold(s) have been adjusted or additional threshold(s) have been added. For the information on the indices calculation and original thresholds, we suggest readers refer to the original publications.

Appendix C. Complexity of changing blue ice states in melt-induced blue ice areas

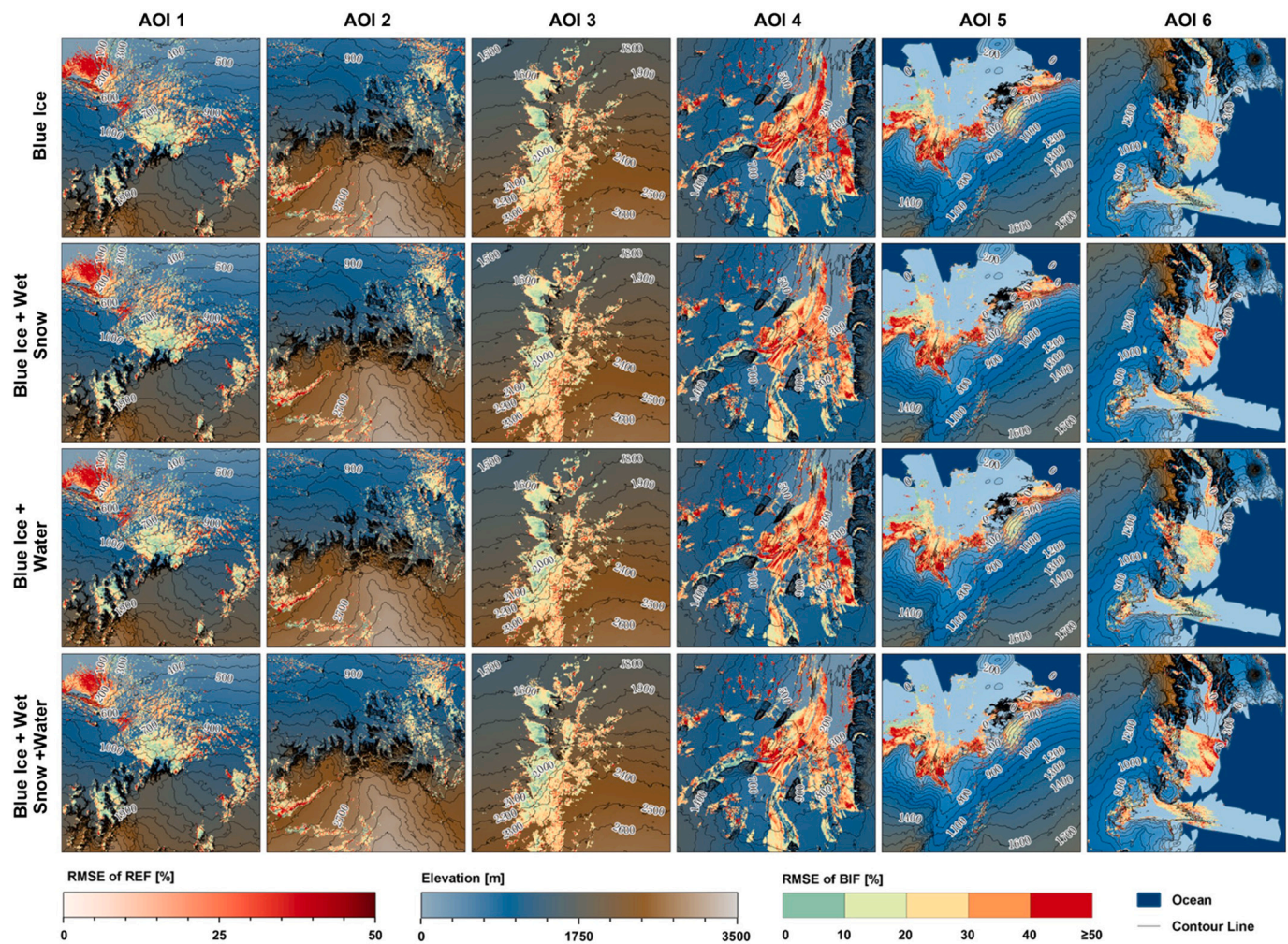


Fig. C.15. The root mean square error of spectral mixture analysis (SMA) results (with different combinations of blue ice, wet snow, and water fractions) from FABIAN (Fractional Austral-summer Blue Ice over Antarctica) in estimating blue ice fractions compared with the Sentinel-2 observations during the austral summer 2018/19 to 2020/21 in each area of interest (AOI): (1) the Petermann Ranges, (2) Sør-Rondane Mountains, (3) Queen Fabiola Mountains, (4) Amery Ice Shelf, (5) Shackleton Ice Shelf, and (6) Victoria Land. (For interpretation of the references to colour in this figure legend, the reader is referred to the web version of this article.)

Appendix D. Agreement among different blue ice area classifiers

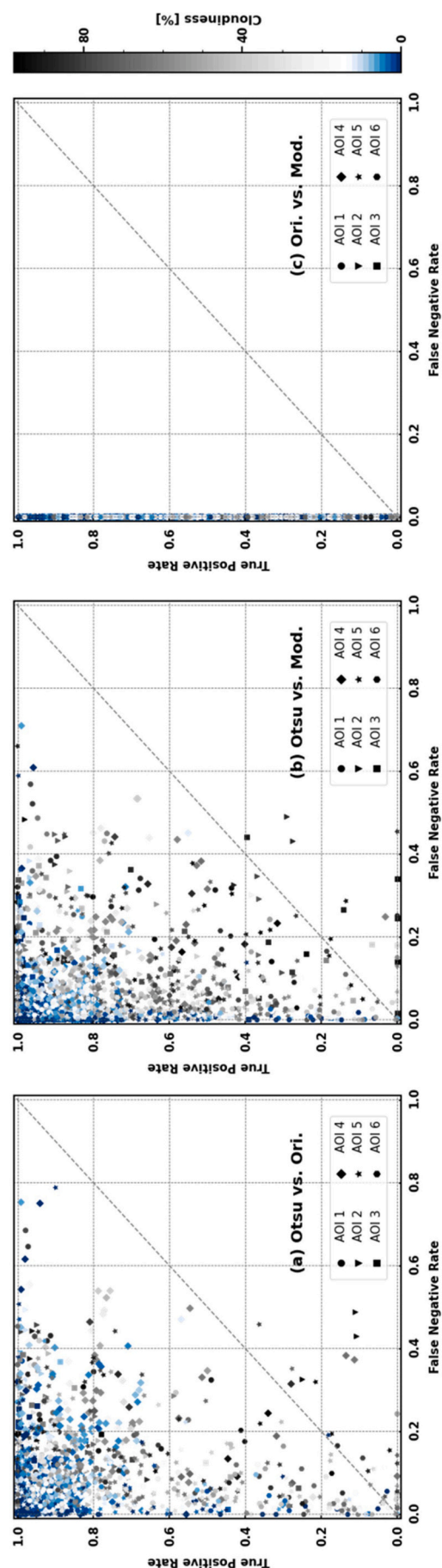


Fig. D.16. Agreement among different blue ice area classifiers based on the original (Ori.) and modified (Mod.) thresholds from Hui et al. (2014), as well as based on the Otsu method (Otsu), under different cloudiness in the exploited Sentinel-2 images in each area of interest (AOI): (1) the Petermann Ranges, (2) Sør-Rondane Mountains, (3) Queen Fabiola Mountains, (4) Amery Ice Shelf, (5) Shackleton Ice Shelf, and (6) Victoria Land, during the austral summer 2019/20 and 2020/21. (For interpretation of the references to colour in this figure legend, the reader is referred to the web version of this article.)

References

- Ackerman, S.A., Strabala, K.I., Menzel, W.P., Frey, R.A., Moeller, C.C., Gumley, L.E., 1998. Discriminating clear sky from clouds with modis. *J. Geophys. Res.-Atmos.* 103, 32141–32157.
- Ackerman, S.A., Holz, R., Frey, R., Eloranta, E., Maddux, B., McGill, M., 2008. Cloud detection with modis. Part ii: validation. *J. Atmos. Ocean. Technol.* 25, 1073–1086.
- Baum, B.A., Menzel, W.P., Frey, R.A., Tobin, D.C., Holz, R.E., Ackerman, S.A., Heidinger, A.K., Yang, P., 2012. Modis cloud-top property refinements for collection 6. *J. Appl. Meteorol. Climatol.* 51, 1145–1163.
- Bell, R.E., Chu, W., Kingslake, J., Das, I., Tedesco, M., Tinto, K.J., Zappa, C.J., Frezzotti, M., Boghosian, A., Lee, W.S., 2017. Antarctic ice shelf potentially stabilized by export of meltwater in surface river. *Nature* 544, 344–348.
- Bindschadler, R., Vornberger, P., Fleming, A., Fox, A., Mullins, J., Binnie, D., Paulsen, S. J., Granneman, B., Gorodetzky, D., 2008. The landsat image mosaic of Antarctica. *Remote Sens. Environ.* 112, 4214–4226.
- Bindschadler, R., Choi, H., Wichlacz, A., Bingham, R., Bohlander, J., Brunt, K., Corr, H., Drews, R., Fricker, H., Hall, M., et al., 2011. Getting around Antarctica: new high-resolution mappings of the grounded and freely-floating boundaries of the antarctic ice sheet created for the international polar year. *Cryosphere* 5, 569–588.
- Bintanja, R., 1999. On the glaciological, meteorological, and climatological significance of antarctic blue ice areas. *Rev. Geophys.* 37, 337–359.
- Bintanja, R., Van den Broeke, M.R., 1995a. The climate sensitivity of antarctic blue-ice areas. *Ann. Glaciol.* 21, 157–161.
- Bintanja, R., Van den Broeke, M.R., 1995b. The surface energy balance of antarctic snow and blue ice. *J. Appl. Meteorol. Climatol.* 34, 902–926.
- Bronge, L.B., Bronge, C., 1999. Ice and snow-type classification in the Vestfold hills, East Antarctica, using landsat-tm data and ground radiometer measurements. *Int. J. Remote Sens.* 20, 225–240.
- Brown, I.C., Scambos, T.A., 2004. Satellite monitoring of blue-ice extent near byrd glacier, Antarctica. *Ann. Glaciol.* 39, 223–230.
- Burton-Johnson, A., Black, M., Fretwell, P.T., Kaluza-Gilbert, J., 2016. An automated methodology for differentiating rock from snow, clouds and sea in Antarctica from landsat 8 imagery: a new rock outcrop map and area estimation for the entire antarctic continent. *Cryosphere* 10, 1665–1677.
- Cheng, X., Zhang, Y., Li, Z., Shao, Y., 2003. Blue-ice domain discrimination using interferometric coherence in antarctic grove mountains. In: *IGARSS 2003. 2003 IEEE International Geoscience and Remote Sensing Symposium. Proceedings (IEEE Cat. No. 03CH37477)*. IEEE, pp. 2599–2601.
- Degerickx, J., Okujeni, A., Iordache, M.D., Hermi, M., Van der Linden, S., Somers, B., 2017. A novel spectral library pruning technique for spectral unmixing of urban land cover. *Remote Sens.* 9, 565.
- Dennison, P.E., Roberts, D.A., 2003. The effects of vegetation phenology on endmember selection and species mapping in southern California chaparral. *Remote Sens. Environ.* 87, 295–309.
- Dennison, P.E., Halligan, K.Q., Roberts, D.A., 2004. A comparison of error metrics and constraints for multiple endmember spectral mixture analysis and spectral angle mapper. *Remote Sens. Environ.* 93, 359–367.
- Dirscherl, M.C., Dietz, A.J., Kuenzer, C., 2021. Seasonal evolution of antarctic supraglacial lakes in 2015–2021 and links to environmental controls. *Cryosphere* 15, 5205–5226. <https://doi.org/10.5194/tc-15-5205-2021>.
- Elmore, A.J., Mustard, J.F., Manning, S.J., Lobell, D.B., 2000. Quantifying vegetation change in semiarid environments: precision and accuracy of spectral mixture analysis and the normalized difference vegetation index. *Remote Sens. Environ.* 73, 87–102.
- Frey, R.A., Ackerman, S.A., Liu, Y., Strabala, K.I., Zhang, H., Key, J.R., Wang, X., 2008. Cloud detection with modis. Part i: improvements in the modis cloud mask for collection 5. *J. Atmos. Ocean. Technol.* 25, 1057–1072.
- Frey, R.A., Ackerman, S.A., Holz, R.E., Dutcher, S., Griffith, Z., 2020. The continuity modis-viirs cloud mask. *Remote Sens.* 12, 3334.
- Gorelick, N., Hancher, M., Dixon, M., Ilyushchenko, S., Thau, D., Moore, R., 2017. Google earth engine: planetary-scale geospatial analysis for everyone. *Remote Sens. Environ.* 202, 18–27.
- Hannula, H.R., Heinilä, K., Böttcher, K., Mattila, O.P., Salminen, M., Pulliainen, J., 2020. Laboratory, field, mast-borne and airborne spectral reflectance measurements of boreal landscape during spring. *Earth Syst. Sci. Data* 12, 719–740.
- Hollstein, A., Segl, K., Guanter, L., Brell, M., Enesco, M., 2016. Ready-to-use methods for the detection of clouds, cirrus, snow, shadow, water and clear sky pixels in sentinel-2 msi images. *Remote Sens.* 8, 666.
- Hu, Z., Kuenzer, C., Dietz, A.J., Dech, S., 2017. The potential of earth observation for the analysis of cold region land surface dynamics in europe—a review. *Remote Sens.* 9, 1067.
- Hui, F., Ci, T., Cheng, X., Scambo, T.A., Liu, Y., Zhang, Y., Chi, Z., Huang, H., Wang, X., Wang, F., et al., 2014. Mapping blue-ice areas in Antarctica using etm+ and modis data. *Ann. Glaciol.* 55, 129–137.
- Libois, Q., Picard, G., France, J., Arnaud, L., Dumont, M., Carmagnola, C., King, M., 2013. Influence of grain shape on light penetration in snow. *Cryosphere* 7, 1803–1818.
- Ligtenberg, S., Lenaerts, J., Van den Broeke, M., Scambos, T., 2014. On the formation of blue ice on byrd glacier, Antarctica. *J. Glaciol.* 60, 41–50.

- Liston, G.E., Bruland, O., Winther, J.G., Elvehøy, H., Sand, K., 1999. Meltwater production in antarctic blue-ice areas: sensitivity to changes in atmospheric forcing. *Polar Res.* 18, 283–290.
- Liu, H., Wang, L., Jezek, K.C., 2006. Automated delineation of dry and melt snow zones in Antarctica using active and passive microwave observations from space. *IEEE Trans. Geosci. Remote Sens.* 44, 2152–2163.
- Matsuoka, K., Skoglund, A., Roth, G., de Pomereu, J., Griffiths, H., Headland, R., Herried, B., Katsumata, K., Le Brocq, A., Licht, K., et al., 2021. Quantarctica, an integrated mapping environment for Antarctica, the southern ocean, and sub-antarctic islands. *Environ. Model. Softw.* 140, 105015.
- Meerdink, S.K., Hook, S.J., Roberts, D.A., Abbott, E.A., 2019. The ecstress spectral library version 1.0. *Remote Sens. Environ.* 230, 111196.
- Mellor, M., Swithinbank, C., 1989. Airfields on Antarctic glacier ice. In: Technical Report. Cold Reg. Res. and Eng. Lab., Hanover, N.H. CRREL Rep. 89-21.
- Orheim, O., Lucchitta, B.K., 1988. Numerical analysis of landsat thematic mapper images of Antarctica: surface temperatures and physical properties. *Ann. Glaciol.* 11, 109–120.
- Orheim, O., Lucchitta, B., 1990. Investigating climate change by digital analysis of blue ice extent on satellite images of Antarctica. *Ann. Glaciol.* 14, 211–215.
- Otsu, N., 1979. A threshold selection method from gray-level histograms. *IEEE Trans. Syst. Man Cybernet.* 9, 62–66.
- Rizzoli, P., Martone, M., Gonzalez, C., Wecklich, C., Tridon, D.B., Bräutigam, B., Bachmann, M., Schulze, D., Fritz, T., Huber, M., et al., 2017. Generation and performance assessment of the global tandem-x digital elevation model. *ISPRS J. Photogramm. Remote Sens.* 132, 119–139.
- Roberts, D.A., Gardner, M., Church, R., Ustin, S., Scheer, G., Green, R., 1998. Mapping chaparral in the Santa monica mountains using multiple endmember spectral mixture models. *Remote Sens. Environ.* 65, 267–279.
- Roberts, D.A., Dennison, P.E., Gardner, M.E., Hetzel, Y., Ustin, S.L., Lee, C.T., 2003. Evaluation of the potential of hyperion for fire danger assessment by comparison to the airborne visible/infrared imaging spectrometer. *IEEE Trans. Geosci. Remote Sens.* 41, 1297–1310.
- Scambos, T.A., Haran, T.M., Fahnestock, M., Painter, T., Bohlander, J., 2007. Modis-based mosaic of Antarctica (moa) data sets: continent-wide surface morphology and snow grain size. *Remote Sens. Environ.* 111, 242–257.
- Sinisalo, A., Moore, J.C., 2010. Antarctic blue ice areas-towards extracting palaeoclimate information. *Antarct. Sci.* 22, 99–115.
- Smith, M.O., Ustin, S.L., Adams, J.B., Gillespie, A.R., 1990. Vegetation in deserts: I. a regional measure of abundance from multispectral images. *Remote Sens. Environ.* 31, 1–26.
- Somers, B., Asner, G.P., Tits, L., Coppin, P., 2011. Endmember variability in spectral mixture analysis: a review. *Remote Sens. Environ.* 115, 1603–1616.
- Tollenaar, V., Zekollari, H., Lhermitte, S., Tax, D.M., Debaille, V., Goderis, S., Claeys, P., Pattyn, F., 2022. Unexplored antarctic meteorite collection sites revealed through machine learning. *Sci. Adv.* 8, eabj8138. <https://doi.org/10.1126/sciadv.abj8138>.
- Trusel, L.D., Frey, K.E., Das, S.B., Munneke, P.K., Van Den Broeke, M.R., 2013. Satellite-based estimates of antarctic surface meltwater fluxes. *Geophys. Res. Lett.* 40, 6148–6153.
- van den Broeke, M., van de Berg, W.J., van Meijgaard, E., Reijmer, C., 2006. Identification of antarctic ablation areas using a regional atmospheric climate model. *J. Geophys. Res.-Atmos.* 111.
- van Wessem, J.M., Reijmer, C.H., van de Berg, W.J., van Den Broeke, M.R., Cook, A.J., van Ulft, L.H., van Meijgaard, E., 2015. Temperature and wind climate of the antarctic peninsula as simulated by a high-resolution regional atmospheric climate model. *J. Clim.* 28, 7306–7326.
- Van Wessem, J.M., Van De Berg, W.J., Noël, B.P., Van Meijgaard, E., Amory, C., Birnbaum, G., Jakobs, C.L., Krüger, K., Lenaerts, J., Lhermitte, S., et al., 2018. Modelling the climate and surface mass balance of polar ice sheets using racmo2—part 2: Antarctica (1979–2016). *Cryosphere* 12, 1479–1498.
- Vikhamar, D., Solberg, R., 2003. Snow-cover mapping in forests by constrained linear spectral unmixing of modis data. *Remote Sens. Environ.* 88, 309–323.
- Williams, R.S., Meunier, T.K., Ferrigno, J.G., 1982. Delineation of blue-ice areas in Antarctica from satellite imagery. In: Workshop on Antarctic Glaciology and Meteorites (Bull. C. and Lipschutz, M.), LPI Tech. Rpt. 82-03. Lunar and Planetary Institute, Houston, p. 49. https://www.lpi.usra.edu/lpi/contribution_docs/TR/TR_8203.pdf.
- Winther, J.G., 1994. Spectral bi-directional reflectance of snow and glacier ice measured in dronning maud land, Antarctica. *Ann. Glaciol.* 20, 1–5.
- Winther, J.G., Jespersen, M.N., Liston, G.E., 2001. Blue-ice areas in Antarctica derived from noaa avhrr satellite data. *J. Glaciol.* 47, 325–334.
- Wu, C., Murray, A.T., 2003. Estimating impervious surface distribution by spectral mixture analysis. *Remote Sens. Environ.* 84, 493–505.
- Yang, K., Smith, L.C., 2012. Supraglacial streams on the Greenland ice sheet delineated from combined spectral–shape information in high-resolution satellite imagery. *IEEE Geosci. Remote Sens. Lett.* 10, 801–805.
- Yoshida, M., Omoto, K., Naruse, R., Ageta, Y., et al., 1971. Discovery of meteorites near Yamato mountains, East Antarctica. *Antarct. Rec.* 39, 62–65.
- Zatko, M.C., Warren, S.G., 2015. East antarctic sea ice in spring: spectral albedo of snow, nilas, frost flowers and slush, and light-absorbing impurities in snow. *Ann. Glaciol.* 56, 53–64.